NTNU

Norwegian University of
Science and Technology

Solving the Inverse Problem of Electrical Resistivity Tomography by Simulated Annealing

Frode Thorsen Børseth

MSc in Physics
Submission date: May 2018
Supervisor: Alex Hansen, IFY

Norwegian University of Science and Technology
Department of Physics

Solving the Inverse Problem of Electrical Resistivity Tomography by Simulated Annealing

Frode Børseth

2018-05-29

Abstract

A detailed account is given of an educational visit with the company Ruden AS, which served as an introduction to the field of Electrical Resistivity Tomagraphy (ERT). The formal Calderón problem is presented afterwards, lying at the basis of ERT. The inverse problem is discretized, phrasing it instead in terms of resistor grids and transfer matrices. The general relation between the transfer matrix and traditional measurements is shown. An algorithm for solving the forward problem is derived, and the strategy for using this to solve the inverse problem is formulated. The minimization algorithm to be used, Simulated Annealing (SA), is described and defined. It is shown to correctly invert surface data into an image of the subsurface structure. The scheme does however demonstrate some limitations, which are discussed.

Sammendrag

En detaljert beretning gis av et lærerikt besøk hos firmaet Ruden AS, som ble en introduksjon til studiet innen Elektrisk Resistivitetstomografi (ERT). Det formelle Calderón problemet, som ligger til grunn for ERT, blir deretter presentert. Inversproblemet blir diskretisert, ved å istedet formulere det ved resistornettverk og transfermatriser. Det generelle forholdet mellom transfermatrisen og tradisjonelle målinger blir vist. En algoritme for å løse frem-problemet blir utledet, og en strategi for å bruke denne til å løse inversproblemet blir formulert. Minimeringsalgoritmen som brukes, "Simulated Annealing" (SA), blir beskrevet og definert. Det blir vist at den på korrekt vis inverterer overflatemålinger til et bilde av den underjordiske strukturen. Prosedyren fremviser imidlertid visse begrensninger, som blir diskutert.

Preface

This thesis is submitted as part of my Master's degree in physics, representing the conclusion of my studies at the Norwegian University of Science and Technology, NTNU. It has been written under the supervision of Prof. Alex Hansen, who was also the one who proposed the problem.

I would like to thank Alex Hansen for the opportunity to work on such an exciting project, which I have found both engaging and rewarding. I would also like to thank him, as well as my fellow student Håvard E. Wiken, for engaging discussions and helpful advice.

I must also give special thanks to Fridjof Ruden of Ruden AS, as well as all the employees at his company, for their kindness and hospitality. Their help at the start of my work has been invaluable, and it was a sincere pleasure getting to know them all.

Finally, I want to give special thanks to my father, for his unending help and support, as well as to the rest of my family. I also want to thank the friends I have gained during my studies who made me feel at home. Without these people, I would not have made it to this point.

Trondheim 2018-05-29

Frode Thorsen Børseth

Table of Contents

List of Tables

List of Figures

List of symbols

∇	Nabla operator
g_n	Conductance of resistor labelled n in grid
$g_{n,m}$	Conductance of resistor between nodes n and m
$g(E)$	Density of states
$g(i\|j)$	Proposal probability
$\mathbf{g}$	Vector of conductances $(g_1, \ldots, g_M)^T$ in resistor grid
$\Delta\mathbf{g}$	Proposed change in grid conductances
i	Microstate
j	(Chapter 3) Neumann boundary condition on u (Chapter 5) Microstate
k	(Chapter 1,2,3) Geometric factor (Chapter 5) Constant, analogous to Boltzmann's constant
k_B	Boltzmann's constant
p	Acceptance probability used in the Metropolis algorithm
$s_E^{(l)}$	Sample standard deviation in the l'th random walk
u	Electric potential
$\mathbf{u}$	Random vector $\in \mathbb{R}^M$, elements from uniform distribution $(-\sqrt{3}, \sqrt{3})$
A	Transfer matrix

A_m	Measured transfer matrix
$A(\mathbf{g})$	Transfer matrix as function of grid conductance vector
$A(i\|j)$	Acceptance probability
$A_i^{(l}$	Average value of the i'th conductance g_i during the l'th random walk
$\mathscr{B}$	Set of boundary nodes
C	Heat capacity of the simulated annealing
C_V	Heat capacity at constant volume
E	Objective function, with interpretation energy
E_i	Energy, or function value, at microstate i
$\overline{E}^{(l)}$	Average energy in the l'th random walk
$E(\mathbf{g})$	Energy, or function value, for grid with conductances $\mathbf{g}$
$\mathbf{E}$	Electric field
$\mathscr{I}$	Set of interior nodes
$\mathbf{J}$	(Chapter 3 [continuous formulation]) Current field (Chapter 3 [discrete formulation], 4) Current vector
K	(Chapter 3,4) Kirchhoff matrix (Chapter 5) Length of random walk
L	Depth of resistor grid
M	Number of conductances that define the resistor grid
N	Number of boundary nodes, or width of rectangular grid
$P(i)$	Probability of microstate i
$P(i\|j)$	Transition probability, from j to i
$S_{i,j}^{(l}$	Second moments of the l'th random walk, with respect to g_i and g_j
T	Temperature

$\mathbf{U}$	Potential vector
Z	Partition function
ρ_a	Apparent resistivity
β	Scaling factor, set to $\beta = 0.11$, used in estimating the covariance matrix s
ϵ	Change in mean energy, $\epsilon = \langle E \rangle_1 - \langle E \rangle_2$
σ	Conductivity
σ_E	Variance of energy
ϕ	Dirichlet boundary condition on u
χ_s	Growth factor of the random walk, set to $\chi_s = 3.0$
χ_T	Annealing parameter, decides energy overlap
Γ	(Chapter 3 [continuous formulation]) Measurable subset of $\partial\Omega$ (Chapter 3 [discrete formulation], 4) Graph of resistor grid
Λ_σ	Transfer function, also called Dirichlet-to-Neumann map
$\partial\Omega$	Boundary of Ω
Ω	Conducting region, as subset of $\mathbb{R}^n$
$\Omega(T)$	Accessible region of phase space

Abbreviations

1D	1-dimension(al)
2D	2-dimension(s/al)
3D	3-dimension(s/al)
ERT	Electrical Resistivity Tomography
EM	Electromagnetic
DtN	Dirichlet-to-Neumann (map)
SA	Simulated Annealing
H2G2	Hitchhikers Guide to the Galaxy

Chapter 1

Introduction

Is it possible to uncover what something looks like on the inside by means of electrical measurements at its surface? The answer to this question, proven by mathematicians only very recently, and known by geophysicists for nearly a century, is "*yes*". The idea has long been applied in practice, in an imaging technique known as *electrical resistivity tomography* (ERT), backed by decades of use, research, and development. Today, software solutions to the problem are commercially available, and have been since the end of the 20th century. But despite a considerable increase in computer power over that time span, the numerical techniques in use remain fundamentally the same as the ones implemented for last-century hardware. This brings us to the goal of this master thesis; to investigate the possibility of interpreting surface measurements by a completely different algorithm.

The history of the ERT method starts in the 1920's with the work of the Schlumberger brothers, making it one of the oldest geohpysical surveying techniques still in use [1]. The measurement techniques and analysis of the early days were quite primitive by today's standards, often relying on overly simplistic assumptions about the investigated geology. But with the advent of personal computers and an ever increasing availability of computational power, this would soon change.

In the latter quarter of the 20th century, numerical techniques were developed for translating surface measurements into subsurface behaviour. As a result, the geophysicist of today has at her disposal powerful inversion software, capable of producing a detailed picture of the subsurface fairly quickly. The industry standard for such software has since the 1990's been the program RES2DINV, which still to this day uses essentially the same numerical techniques as twenty years ago. Today, ERT is a widespread imaging technique, and has been used for decades in the fields of hydrogeology, mining, geotechnical, environmental, and hydrocarbon exploration [1]. Chapter 2 recounts a visit with the company Ruden AS, in which the concepts involved in modern day ERT measurements and data analysis are presented in detail.

Meanwhile, the first rigorous mathematical formulation of this problem was published by the Argentinian mathematician Alberto Calderón in the year 1980 [2]. His seminal paper sparked much interest in the subject, still ongoing to this day, both

on its mathematical properties as well as the development of numerical solutions. The problem is today commonly known by his name, as the *Calderón problem* [3], and chapter 3 will explore its formulation and relevant findings.

It is important to understand that the problem at hand, being a so called *inversion problem*, is severely ill-posed (SOURCES). Numerical solutions typically treat it as an optimisation problem, to minimise the difference between measurements and the response of a simulated model. However, in order for traditional optimisation algorithms to be applicable, the problem must be regularised in some way. In the context of ERT, this is achieved by designing the measurements to be sensitive to specific kinds of behaviour in the subsurface, while other approaches rely instead on discretizing the subsurface optimally [4]. In this thesis, we take a different approach.

The *simulated annealing* (SA) method has proven to be very successful at solving a wide variety of difficult problems. While it can be far more computationally costly than traditional optimisation algorithms, it makes up for this in its generality and resistance to ill-posed problems of high difficulty. For instance, it has proven particularly resilient against hard combinatorial problems, where the concept of a "steepest decent" may well not even apply, as well as badly behaved functions of many variables and multiple local minima, where local optimisation is unsafe.

It would seem that SA is our ideal algorithm, as its strengths happen to overlap precisely with the challenges posed by the Calderón problem. In fact, the idea of using SA to solve an inverse problem is not without precedence [5, 6, 7, 8], and with such a body of work documenting its success, this proposition does not only seem true; it seems obvious.

For these reasons, this thesis aims to explore the possibility of using SA to numerically invert ERT data. The scope will be limited to simplified models and measurements, on small scales and in purely two dimensions, as covered in chapter 4. This restriction will make it possible to arrive at real answers within the time constraints involved with a masters thesis, while still retaining the characteristic behaviour of the inverse problem of ERT. The method of SA is discussed in chapter 5, along with a description of the particular implementation used in the numerical experiments. Finally, based on the results presented in chapter 7, the relevant findings will be discussed in chapter 8, ending in a conclusion to the research question of this thesis: Can the Calderón problem be solved numerically by simulated annealing?

Chapter 2

Field work at Ruden AS

I was invited to visit the company Ruden AS for three days in October of 2016, from Sunday the 2nd to Wednesday the 5th. While visiting, I was given the chance to learn about electrical resistance tomography (ERT), to practice with their equipment, and to observe and participate in their work. I joined them for one of their assignments, in which they were to investigate the subsurface of a residential area at Strøm Terrasse, Drammen, using, amongst other techniques, ERT. This visit, having been my introduction to this exciting field at the start of my work, makes for a natural place to start this thesis, and a good introduction to the core concepts of inversion theory.

The company, named after its founder and owner Fridtjov Ruden, was established in 2007, and has since been praised for great innovation within the fields of geology and hydrogeology.[9] While their offices are located in Engelsviken, Norway, demand for their work has taken them to many different countries across several continents.

Central to the company's philosophy is the belief in "sensible usage of science and technology", which has greatly impacted their business. While the techniques and technologies that they rely on have strong ties to the oil industry, their work aims to instead use these tools to the benefit of the environment. Their experience in using ERT-measurements for various geological surveys is only one example of this.

After my arrival at Engelsviken on Sunday the 2nd of October, I would have three days for gaining experience with the practical side of ERT. On Monday, I would join them in practicing with the equipment, and on the two subsequent days I would follow and participate in one of their assignments at Strøm Terrasse, Drammen.

During both the Monday trial run and the assignment at Strøm Terrasse, there would be great opportunity to see the many difficulties that may appear in real life measurements. While the Monday practice run would teach me the workings of the equipment, the following days would give experience with doing measurements.

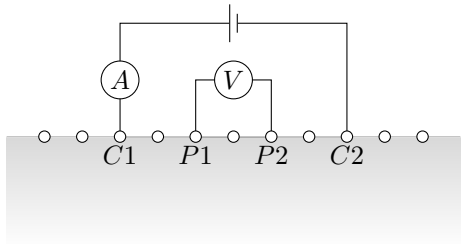

Figure 2.1: A quadripole configuration to measure apparent resistivity.

2.1 ERT measurements

In short, ERT measurements involve placing electrodes in the ground at various positions, and measuring how well the earth conducts current between them. The hope is that, with the right kind of measurements and enough of them, it might be possible to say something about what is underneath the surface.

Typically the electrode positions are fixed, and the number of electrodes in use can be very large. The measurement process itself is automated by so called imaging resistivity meters, so that most of the actual physical labour takes place during the preparatory work of setting up the equipment.

In a typical setup the electrodes are spread out along a straight line, and the measurements are used to create a 2D cross-sectional image. This imaging technique assumes that the conductance only varies along the line and downward, and not in the direction perpendicular to the measurements. If the subsurface is suspected to have a very irregular structure, the electrodes may also be placed in a grid on the surface, in order to create a 3D image of the subsurface.

A set of surface measurement data contains multiple recorded values of what is known as the *apparent resistivity*, denoted ρ_a. Each value is computed from electrical measurements involving four electrodes at the same time. An example configuration of electrodes is presented in figure 2.1. Two electrodes are used to pass a current I through the ground, and they are labeled $C1$ and $C2$. The other two electrodes measure the resulting potential difference V at positions labeled $P1$ and $P2$. The four positions $C1, C2, P1, P2$ are always distinct points.

The apparent resistivity ρ_a is that which would be needed in a homogeneous subsurface for it to produce those same measured values for the same configuration of electrodes. It can easily be calculated from I and V, given that we know the distance between all of the electrodes, by

$$\rho_a = k\frac{V}{I} \tag{2.1}$$

where k is a geometric factor depending on the electrode configuration. Denoting

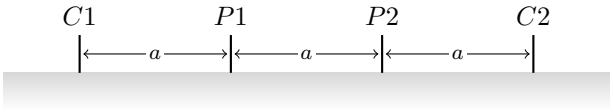

(a) Wenner

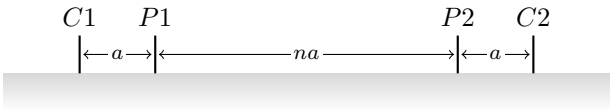

(b) Dipole-dipole

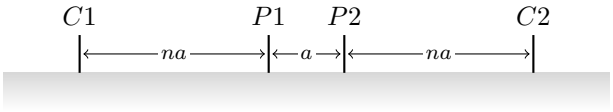

(c) Wenner-Schlumberger

Figure 2.2: Relative positions of electrodes in the different quadripole arrays.

the distance between electrode A and B by r_{AB}, the expression for k becomes

$$k = 2\pi \left(\frac{1}{r_{C1P1}} - \frac{1}{r_{C2P1}} - \frac{1}{r_{C1P2}} + \frac{1}{r_{C2P2}} \right)^{-1},$$

derived in appendix A.

Evidently, the geometric factor k can take many values, as there are many different ways of arranging these four electrodes, both in spacing and relative positions. Schemes for altering these in a regular way exist, for which k has known and simple expressions depending on the distance between the electrodes. These schemes are referred to as quadripole arrays, and the most common have specific names.

Depending on the type of behaviour that we would like to uncover in the subsurface, we would choose a specific kind of quadripole array. Below is a short description of the most important ones. For a more thorough discussion on their properties, see [1, pp. 31-43].

- The **Wenner** array: One of the earliest quadripole arrays used in 2D surveys, the Wenner array is said to be quite robust. Its depth of investigation is described as "moderate", but its relatively low k means that the signal strength is good.

  The quadripole configuration is seen in figure 2.2a, where it is clear that all electrode spacings are given by the distance a. While it is good at detecting vertical changes in the subsurface, it is not as sensitive to horizontal changes.

Array	k	H-sensitivity	V-sensitivity
Wenner	$2\pi a$	bad	good
Dipole-dipole	$\pi n(n+1)(n+2)a$	good	bad
Wenner-Schlumberger	$\pi n(n+1)a$	moderate	moderate

Table 2.1: Summary of properties for the three mentioned quadripole arrays

- The **Dipole-Dipole** array: The dipole-dipole array is widely used because of two reasons: Its measurements are less noisy because of low EM-coupling in the circuitry, and it is ideal for detecting horizontal variations, like e.g. smaller cavities.

  The "dipole" name refers to how the electrodes are placed in separated pairs, as seen in figure 2.2b. The current electrodes are placed next to each other, as are the potential electrodes, with a larger distance between the two pairs.

- The **Wenner-Schlumberger** array: A hybrid between the previously mentioned Wenner array and the Schlumberger array (the Schlumberger array will not be discussed here). This array can in many ways be described as a compromise between the Wenner and Dipole-dipole arrays. While the latter two offer either good horizontal or vertical cover, the Wenner-Schlumberger array falls somewhere in between, being serviceable in both respects. Its electrode configuration is seen in figure 2.2c.

Table 2.1 gives a summary of these different quadripole arrays and their properties, including their respective expressions for k.

Apparent resistivities are typically presented graphically in what is called a pseudosection, a 2D color plot of every measurement value, as seen in the top of figure 2.6. Measurements from electrodes spaced close together are depicted as higher up in the colour plot, while the horizontal position of each measurement is defined by the midpoint of its set of electrode locations.

While pseudosections give a good picture of the apparent resistivities, they do not give any clear indication of what the subsurface actualle look like. This is only revealed upon inversion of the measurement data, and the two pictures will not look the same.

Once the measurements have been made, they are processed by so called "inversion"-software, used to invert the image we have made of the surface behaviour into an image of the subsurface behaviour. The industry standard is the program RES2DINV, developed by geophysicist M.H. Loke and provided by his company Geotomo Software. He has worked on the numerical methods involved in the program since his 1994 PhD thesis until today, and based the program on his findings.

The program RES2DINV supports measurements made using any quadripole array when properly input to the program. Measurements are listed in a large file, where each measurement's electrode positions and apparent resistivity value is given its own line.

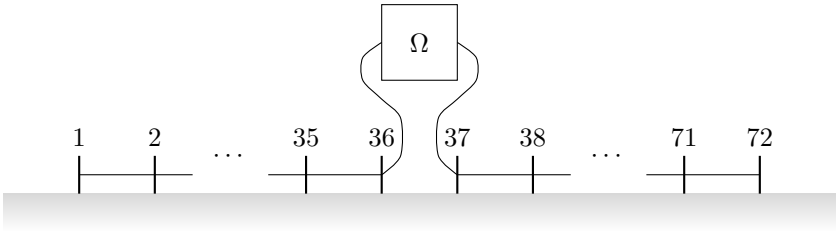

Figure 2.3: Schematic of measurement setup with 72 electrodes, cables, and resistivity meter.

As for the practical side of ERT measurements, the data collection process consists of two stages. First, electrodes are placed a set distance d apart in a line along the stretch of land to be investigated. For a given quadripole array, like the ones in figure 2.2, the factor a becomes an integer multiple of d. As is illustrated in figure 2.3, these are then connected to a cable running along the electrodes, which in turn is connected to a large box near the middle of the line, called an imaging resistivity meter. It is this box that in the end performs all the measurements.

Second, once all the equipment is in place, the resistivity meter is switched on, and after choosing the correct sequencing option (which has to be programmed beforehand) the measurements start. The resistivity meter is able to rapidly switch between the many electrodes connected to it, measuring ρ_a for all the preprogrammed quadripoles. To be clear, there are two cables, one for each direction out from the centre of the line, but one would only ever see one cable at a time walking past the electrodes.

While laying out the cable along the electrodes, care has to be taken so that it does not at any point lay in loops. Such loops would introduce potentially non-negligible inductors in our circuits, which would greatly affect the quality of the measurements.

2.2 Engelsviken and Strøm Terrasse

On Monday, a trial run was organized in Rudens back yard, specifically to teach me the basic procedures of ERT measurements. We were measuring a flat stretch of land, as simple as it gets for making ERT measurements. There was plenty of room for the equipment, without any obstacles to navigate, so that the only concern was to make sure the electrode positions were correct.

We used the same equipment during the trial run as on the following days, the same electrodes and cables. We also chose the quadripole array Wenner-Schlumberger both for the monday trial and on the two subsequent days. The imaging resistivity meter was an IRIS Syscal with 72 electrode connections, 36 in both directions, but for simplicity and in order to save time, we used only half the typical number of electrodes on monday. This meant using just one of the two electrode cables, and as a result significantly reducing the measurement time.

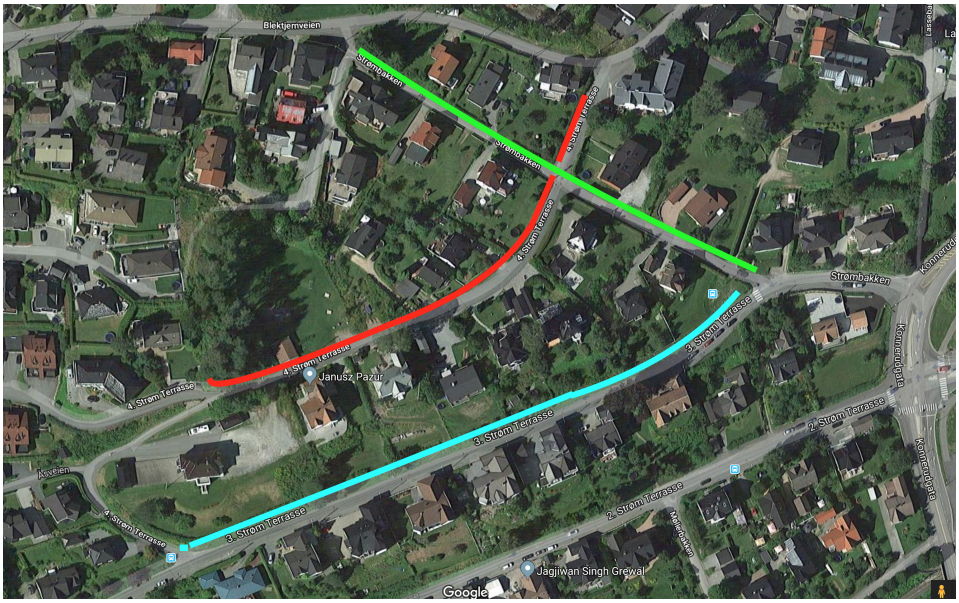

Figure 2.4: A map of Strøm Terrasse, Drammen, along with three coloured lines indicating where our measurements were taken.

(a) Electrode

(b) IRIS Syscal

(c) Me at Strøm Terrasse

Figure 2.5: Footage from the assignment at Strøm Terrasse.

The two following days I was brought along for an assignment in the city Drammen, a short drive from the Ruden AS offices in Engelsviken. Our task was to perform a geological survey in the middle of a residential area, fittingly named "Strøm Terrasse".

One of the real advantages of ERT as a surveying technique, which was made quite apparent by this assignment in particular, is its non-invasiveness. Despite the challenges posed by the large amount of houses and gardens that covered this piece of land, as well as the people living there and attending to their daily lives, we were able to perform all the ERT measurements we needed. Furthermore, we were able to do so with relative ease, and without hardly any disturbance to the residents during our time there.

However, this is not to say we did not encounter any problems at all. For instance, we were only to conduct measurements along the streets of the neighbourhood. And as is evident from figure 2.4, particularly in the red line, these were not always straight. One will always face these kinds of problems in practice, especially on smaller scales, and as a consequence electrode placements are never completely precise.

The inversion software was said to be sufficiently robust that small deviations would be negligible and no reason for concern. The program RES2DINV also allows for positions and heights of each electrode to be specified, and so these were measured using a GPS. This additional data could be used to account for irregularities in height and distance in order to improve the inversion results.

The electrode spacing was not the same in all three measurement runs. In each case it was calculated using the length of the street and the number of electrodes in our array, being 72. For the red line, this meant a spacing of 3 meters, whereas for the green and blue we used 3.5 meters. Note, however, that the green line is far shorter than the blue. This was because it was intended to stretch further upwards in the map, but doing so would require stretching the cable across a long section of asphalt, and boring several holes for the electrodes placed in that region. In the end the decision was made to cut the line short, and instead lose a few measurement points.

In fact, some measurement points were lost in all three of the runs. In all three we found that there was no room at the end of the line for the last few electrodes. Similarly, we were at times forced to leave an electrode site unconnected in the middle of the line, as in cases where the position of an electrode was on top of someones driveway. These dead electrodes were all handled by the Syscal resistivity meter at the start of the measurements, as it would check which were conducting and which were not.

For electrodes that did not seem well connected to the soil, either by inspection or by direct measurements from the Syscal, salt-water sometimes served as a quick fix. The solution was poured on and around the electrode, with surprisingly good results.

Each measurement series took a long time to complete, about 2 hours, depending on the number of electrodes. Also, at one point the apparatus randomly failed and lost all progress, forcing us to restart it. The team used the time between

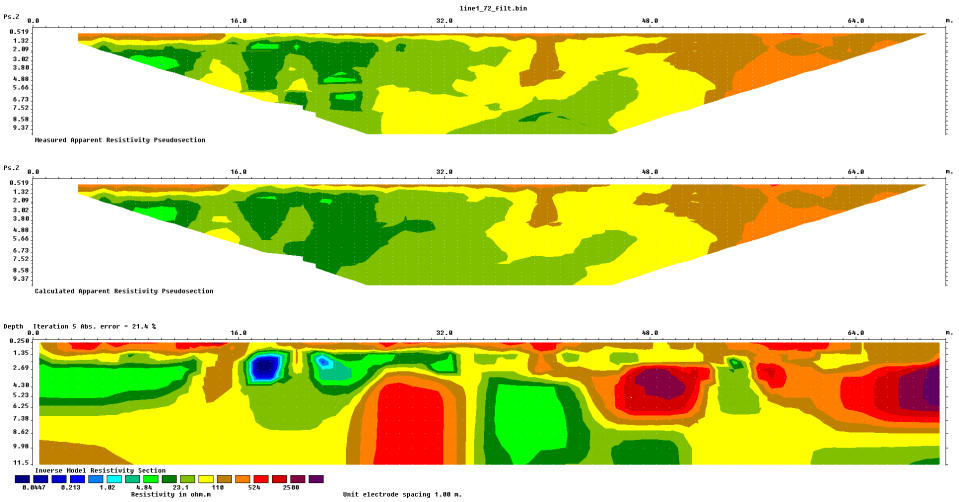

Figure 2.6: Example of RES2DINV output, with measured and simulated pseudosections and the inverted picture (data provided by Ruden AS)

measurements to set up the next array of electrodes in the correct locations, not to mention that there was at the same time several other kinds of surveying techniques being performed.

2.3 The inversion software

After the trial measurement on Monday, I was given a demonstration of the inversion software used to make pictures of the subsurface, applied on data that had been recorded at a previous assignment. The RES2DINV program used for inversion is maintained by the company Geotomo Software, owned by M. H. Loke. It is proprietary software, and requires a software license in order to be used, which is sold in the form of a USB-drive. Without the USB-drive, the program does not give the user permission to apply the inversion on their ERT-data.

The software generates three images from the measurement data, as can be seen in figure 2.6. It produces a pseudosection of the measured apparent resistivities, a pseudosection of the apparent resistivies of the model subsurface, as well as an image of the inversion result. Figure 2.6 presents the measurements and inverted image of the example data that was provided by Ruden.

In the pseudosection, the apparent resistivities are mapped to a 2D image in a manner consistent with where they were recorded and the electrode spacing that was used. Resistivities recorded using wider electrode spacings are shown as being "deeper down" in the pseudosection, mirroring how these measurements "see" deeper into the ground, while short spacings are higher up. Because fewer measurements are possible with a wider electrode spacing, the border of the pseudosection slants inward towards the bottom.

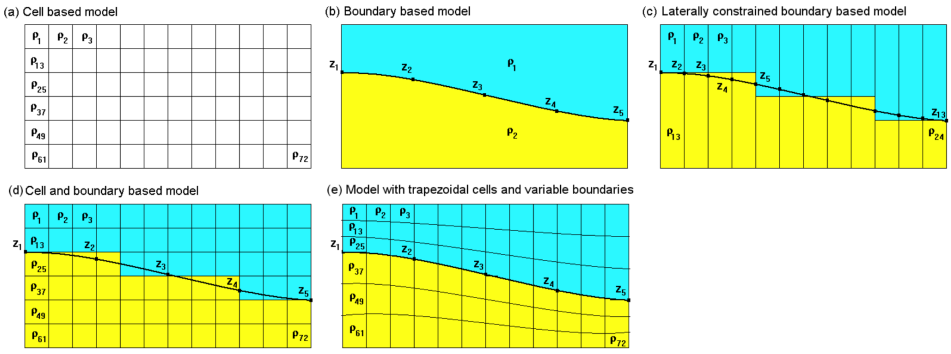

Figure 2.7: Illustrations of different block models available in RES2DINV. [1, p 16]

Pseudosections are useful for visualizing the recorded data, but they are not representative of the actual subsurface structure. The two images are practically guarranteed to look very dissimilar, though they may display patterns that appear correlated.

In the model used by the program, the subsurface is divided into many blocks. The exact structure, the size and way these blocks make up the subsurface, can be handled in a variety of ways, as seen in figure 2.7. Each block is given a resistivity, which become the variables of the inversion.

For such block-like structures, the forward problem has solutions provided by the finite-difference method [10][1, p. 11]. That is, given the resistivity of each block, it is possible to compute the apparent resistivities that would have been measured at the surface. Doing this gives the program a way to compare the proposed model with the measurement data, and evaluate the error by computing their difference.

The inversion in RES2DINV is essentially a minimisation of this error, where the resistivity of the many blocks are the variables of the minimisation. Crucially, the minimisation algorithm used is a quasi-Gauss-Newton least-squares method, a fact that will be brought up again in chapter 5. It attempts to find the zero of the vector function $\mathbf{g}$, whose elements are the error between measured and simulated apparent resistivities, and whose argument is the vector of block resistivities $\mathbf{q}$ [1, pp. 10-14]. The program finds the zero of $\mathbf{g}$ by the scheme

$$\mathbf{q}_{k+1} = \mathbf{q}_k + \Delta\mathbf{q}_k \tag{2.2}$$

$$(J^T J + \lambda F)\Delta\mathbf{q}_k = J^T\mathbf{g} - \lambda F\mathbf{q}_k \tag{2.3}$$

where J is the Jacobian matrix, while the dampening factor λ and smoothness-constraining matrix F make sure that the resistivity distribution remains well behaved with each iteration.

The program also allows for further modifications to this scheme. If for instance the subsurface is known to have sharp transitions between different media, the program can instead apply a least-absolute-error method for specific regions. The program also is able to handle time-dependent measurements, which require further alterations to the minimisation scheme.

Furthermore, the user is allowed to control a number of parameters in the minimisation, like the number of iterations to be performed, or how many parameters are to be used in the subsurface model. It is also possible to set whether to directly minimise the difference in ρ_a, or whether to minimise the difference between the logarithms, that is $\ln(\rho_a)$, where it is most common to use the latter option.

As should be clear, the software is quite powerful and comprehensive, and it is difficult to give a complete account of its abilities. For a complete tutorial on the program RES2DINV, see [1].

2.4 Summary of visit

During my visit at Ruden AS, I was taught the basics of professional ERT surveying. The first day was spent practising and becoming familiar with the equipment and instruments. The second and third day I was taken along on one of their assignments, was allowed to participate in the measurement process, and saw first hand the many strengths of ERT, as well as some of the subtle problems it may encounter.

In addition to seeing the field work involved in this imaging technique, I was given a demonstration of the inversion software used to interpret our measurements. The program RES2DINV is the industry standard for inverting ERT-data, and my time at Ruden AS gave me great insight into the abilities and inner workings of this powerful software.

Chapter 3

The inverse problem

Having built some intuition in the previous chapter, we can now move on to phrase the problem of ERT more formally. This will involve moving away from the comforts of simple electrode arrays and tangible measurements, and on to more abstract mathematical objects as part of the discussion. But only for a short while, as the link between these abstract objects and simpler electrode measurements will be tied soon after.

In the mathematical literature, the inverse problem of ERT is known as the "Calderón problem", after the mathematician who brougt attention to it in 1980 [2]. First in this chapter, a description of the Calderón problem will be presented, with some history, as well as a short review of the relevant findings that have been made over the last few decades. Then, the problem will be discretized, in order to consider measurements at finitely many points on the surface, and introducing a resistor grid model of the subsurface.

3.1 The Calderón problem

To build up the framework of concepts involved in Calderón's problem, it is useful to start with a review of electrostatics. First of all, an electric potential u gives rise to an electric field $\mathbf{E}$ by

$$\mathbf{E} = -\nabla u. \tag{3.1}$$

The electric field in turn is related to the current field $\mathbf{J}$ by Ohms law,

$$\mathbf{J} = \sigma \mathbf{E} \tag{3.2}$$

where σ is the conductivity. In general, all of the above are functions of position.

If there are no sources of current in a particular region of space, we have that $\nabla \mathbf{J} = 0$, and as a consequence

$$\nabla \cdot \sigma \nabla u = 0 \tag{3.3}$$

in that same region. This differential equation determines the shape of u, when accompanied by boundary conditions. Note that for uniform conductance, equation (3.3) simplifies to Laplace's equation, $\nabla^2 u = 0$.

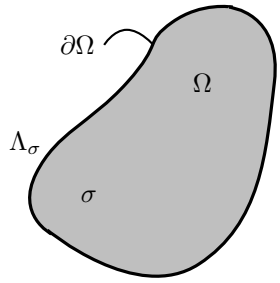

Figure 3.1: An illustration of the conducting region Ω, with surface $\partial\Omega$, conductance σ, and the DtN-map Λ_σ.

In the interest of generality, consider now some electrically conductive n-dimensional region $\Omega \subset \mathbb{R}^n$, illustrated in figure 3.1, with conductance given by σ, and without any charges or sources of current in its interior. Because we are interested in performing electrical measurements on $\partial\Omega$, it will be fruitful to consider the different kinds of boundary conditions we may place on u. For instance, the set of equations

$$\nabla \cdot \sigma \nabla u = 0 \quad \text{in } \Omega \tag{3.4}$$

$$u|_{\partial\Omega} = \phi \quad \text{on } \partial\Omega \tag{3.5}$$

the second of which is the boundary condition, will completely determine u inside Ω. The function ϕ above is what is called a Dirichlet boundary condition, because it fixes the value of u itself at the boundary.

We could also have used as boundary condition some constraint on the derivative of u in a direction $\mathbf{n}$ perpendicular outward from $\partial\Omega$, set equal to some function j, by

$$\big(\mathbf{n} \cdot \sigma \nabla u\big)\big|_{\partial\Omega} = j \quad \text{on } \partial\Omega. \tag{3.6}$$

This type of constraint is known as a Neumann boundary condition, fixing the derivative instead of the value of u itself. Note that the expression above in fact is the normal component of the electric current directed into Ω,

$$\big(\mathbf{n} \cdot \sigma \nabla u\big)\big|_{\partial\Omega} = \big((-\mathbf{n}) \cdot \mathbf{J}\big)\big|_{\partial\Omega} = j. \tag{3.7}$$

Once a boundary condition has been imposed, be it Dirichlet or Neumann, the potential u is determined, and we are free to find and evaluate both it and its derivatives at the boundary. It should then be clear that it is possible to find pairs ϕ and j that will both result in the same solution u.

Because any electrical measurement involves finding a relation between imposed potentials and currents, the relationship between such function pairs is relevant

to our problem. With this in mind, consider the map Λ_σ between such pairs of boundary conditions:

$$\Lambda_\sigma : \phi \mapsto \left(\mathbf{n} \cdot \sigma \nabla u\right)\big|_{\partial\Omega} \tag{3.8}$$

Such a map contains a lot of information, as it completely characterises the behaviour of $\partial\Omega$ when subject to electrical stimuli [4]. As such, it is a kind of *transfer function* for the body Ω, transferring an imposed potential function to the electrical current response. In the literature this transfer function is most commonly referred to as a Dirichlet-to-Neumann map, or DtN-map for short [3]. Given such a DtN-map, one would be able to predict the outcome of any conceivable electrical measurement made on $\partial\Omega$. Naturally, the DtN-map Λ_σ will depend on the conductivity σ of Ω, hence the subscript.

The DtN-map can also be thought of as the sum of all information retrievable by means of electrical surface measurements, or the data one would be able to collect from an infinite number of measurements using equipment with infinite resolution. It therefore is the perfect object for representing a complete set of surface measurements.

It might be clear at this point that the inverse problem in question generally considers the relationship between measurements of Λ_σ and the conductance σ. While the introduction above fails to specify several details, like the permitted behaviour of the function σ and so on, it still has gotten us to the point where we may phrase a simplified version of the Calderón problem:

> Recover the conductivity σ of a body Ω from its Dirichlet-to-Neumann map Λ_σ.

While this essentially is the Calderón problem as it is phrased today, it should be noted that Calderón himself in his seminal 1980 paper [2] took a different approach. Instead of phrasing the inverse problem in terms of Λ_σ, he considered measurements of the quadratic form[1] Q_σ, defined as

$$Q_\sigma(\phi) = \int_\Omega \sigma(\nabla u)^2 \mathrm{d}x.$$

In later years, however, the problem has come to be more typically phrased in terms of the DtN-map Λ_σ.

3.2 Findings since Calderón

Since Calderón's publication in 1980, a number of results have been produced, both addressing the question posed above, as well as some that are still closely related. This section will review some of the more salient findings, but for a more complete account of the history, see e.g. [3] or [4].

[1] The physical interpretation of $Q_\sigma(\phi)$ is the power dissipated in the conducting body in order to maintain the boundary potential ϕ.

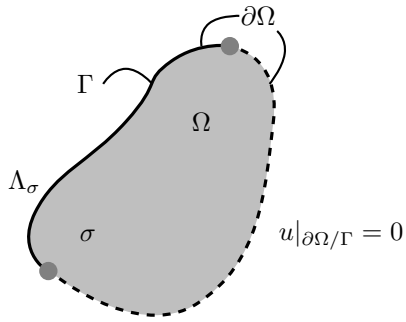

Figure 3.2: Partial boundary setups.

What was not initially known even by Calderón was whether the conductivity was uniquely determined by the DtN-map. That is, for two functions σ_1 and σ_2, does $\Lambda_{\sigma_1} = \Lambda_{\sigma_2}$ imply $\sigma_1 = \sigma_2$? This was proven to be the case in 1988 for the 3D problem by Sylvester-Uhlmann [11], and quite generally for the 2D case in 2006 by Astala-Päivärinta [12], with several previous results for various smoothness criteria on σ.

But that alone is not sufficient for us to hope that the inverse problem can be solved. One must also consider the stability of the solutions. That is, if Λ_{σ_1} is close to Λ_{σ_2}, is it true that σ_1 is close to σ_2, in some suitable sense? After all, for ill-posed inverse problems that is quite often not the case.

One result, from 1988 by Alessandrini [13], states that given two sufficiently regular conductivities σ_1 and σ_2, the best possible stability estimate is of logarithmic type

$$\|\sigma_1 - \sigma_2\| \leq c \left|\log\left(\|\Lambda_{\sigma_1} - \Lambda_{\sigma_2}\|\right)\right|^{-\alpha} \tag{3.9}$$

for some positive constants c and α and appropriate norms of σ and Λ_σ. This bound did not bode well, as in plainer terms it implies a need for exponential precision in Λ_σ in order to get polynomial precision in σ. A later result by Alessandrini-Vessella from 2005 [14] would seem more optimistic. They proved, for conductivities that are piecewise constant on a finite number of subdivisions of Ω, that the bound above instead becomes of Lipschitz type,

$$\|\sigma_1 - \sigma_2\| \leq C\|\Lambda_{\sigma_1} - \Lambda_{\sigma_2}\|. \tag{3.10}$$

However, as Alessandrini-Vessella themselves stated, this bound did by no means imply any sort of well-posedness. And true enough, the Lipschitz constant above was later shown by Rondi in 2006 [15] to grow exponentially with the number of subdivisions. Thus there is no doubt that the Calderón problem is indeed severely ill-posed.

Yet another interesting aspect is that of measurements with partial data, as illustrated in figure 3.2. Consider the case where only a subset $\Gamma \subset \partial\Omega$ is measurable,

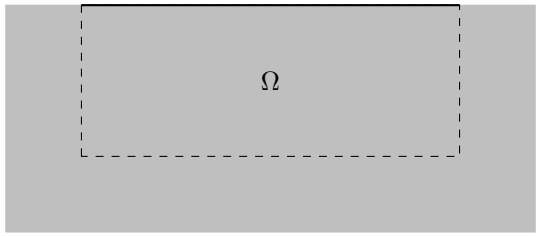

Figure 3.3: An illustration of the subsurface in ERT measurements, where the dashed line represents the imagined extended boundary at which the potential is approximately zero.

while the rest of the boundary $\partial\Omega/\Gamma$ is grounded, i.e. $u|_{\partial\Omega/\Gamma} = 0$. Then, if $\Lambda_{\sigma_1}(f)|_\Gamma = \Lambda_{\sigma_2}(f)|_\Gamma$ for all partial boundary voltages f, do we still have $\sigma_1 = \sigma_2$?

The most recent result in this context is that by Imanuvilov et al. from 2010 [16], which proved uniqueness in general for the 2D partial boundary setup, provided the measured part of the boundary makes up a sufficiently large portion of $\partial\Omega$. The same was proven for dimensions $n \geq 3$ in a result by Kenig et al. from 2007 [17], however it still relied on a smoothness constraint on σ.

The partial boundary problem is particularly relevant for the geophysical application of ERT. Consider the subsurface illustrated in figure 3.3. For surface measurements on the black line, the electric field in the ground quickly falls to zero away from the electrodes. At an imagined boundary located at a sufficiently deep depth and long distance away, the dashed border can to a good approximation be considered grounded, and so the results mentioned above apply.

These analytic results are reassuring with respect to practical applications. However, they do not help us directly in the context of discrete measurements treated by a computer. In order to solve Calderón's problem numerically, we will have to discretize the concepts above, both the conducting body Ω and conductivity σ, its surface $\partial\Omega$, as well as its transfer function Λ_σ. The equations of electrostatics will then no longer be directly applicable, so we must rephrase these as well in discrete terms. Fortunately, a convenient and familiar discrete equivalent will present itself quite naturally, in the form of Kirchhoff's circuit laws.

3.3 Discrete measurements on $\partial\Omega$

As was covered in chapter 2, the quantity of interest in geophysical ERT measurements is the apparent resistivity ρ_a, and it is measured from four points on $\partial\Omega$. This kind of measurement might appear to be far removed from the more abstract transfer function, which was defined for the entire boundary simultaneously instead of only four points. It is not immediately apparent that one can be found from the other. Yet it was stated that Λ_σ completely defined the response of Ω to any boundary condition, and so for any kind of electrical measurement. As will be made clear in this section, this even applies for measurements made on discrete points, or electrodes, on the surface.

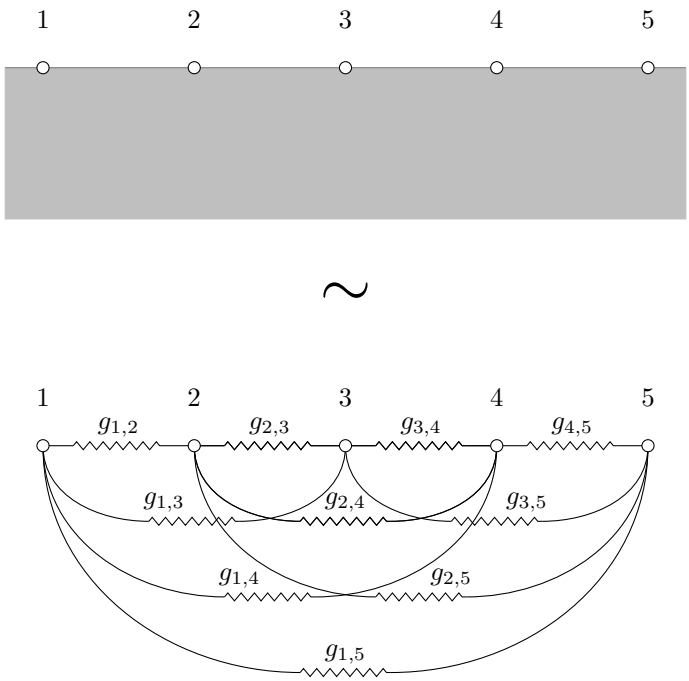

Figure 3.4: Above: a continuous medium with 5 electrodes at its top border. Below: a web-like resistor grid, with one resistor of conductance $g_{n,m}$ between each pair of nodes (n, m). Values for $g_{n,m}$ can always be found so that the two have indistinguishable behaviour.

Let us start by restricting our measurements to N points, or electrodes, on $\partial\Omega$, as shown in the top half of figure 3.4. We may then place potentials U_n on the electrodes n, measure the resulting currents J_m, and define the two vectors

$$\mathbf{U} \equiv (U_1, \ldots, U_N)^T, \tag{3.11a}$$

$$\mathbf{J} \equiv (J_1, \ldots, J_N)^T. \tag{3.11b}$$

Because the transformation between potentials and currents is *linear*[18], these two vectors are related by a matrix that we will denote A;

$$A\mathbf{U} = \mathbf{J} \tag{3.12}$$

This is the discrete equivalent of the transfer function Λ_σ, and it is referred to as the *transfer matrix* of the system. Without going into detail (for the curious, see [19]), the matrix A can be computed from the transfer function Λ_σ using only the position of the measurement points on the surface $\partial\Omega$.

Before relating this transfer matrix A to measurements of ρ_a, it will be useful to learn some more about it and its properties, like whether it is invertible, or what a physical interpretation of its elements might be. To that end, while it may

initially seem unrelated, consider the web-like resistor grid in figure 3.4. Let its nodes be labeled 1 to $N = 5$, and suppose we impose a potential vector $\mathbf{U}$ on these to measure currents $\mathbf{J}$. The resistor from n to m has conductance $g_{n,m}$, and the current running through it from n to m we denote $I_{n,m}$, while its drop in electric potential is $V_{n,m}$. Then by Ohms law we have

$$I_{n,m} = g_{n,m} V_{n,m} \tag{3.13}$$

If we define the potential drops $V_{n,m}$ in terms of the imposed potentials U_i, by $V_{n,m} = U_n - U_m$, Kirchhoff's voltage law is automatically satisfied. Furthermore, Kirchhoffs current law tells us that

$$\sum_{\substack{m=1 \\ m \neq n}}^{N} I_{n,m} = J_n \tag{3.14}$$

and putting all of these three equations together, we get

$$\sum_{\substack{m=1 \\ m \neq n}}^{N} g_{n,m}(U_n - U_m) = J_n \tag{3.15}$$

and after rearranging slightly this becomes

$$\left(\sum_{\substack{m=1 \\ m \neq n}}^{N} g_{n,m} \right) U_n + \sum_{\substack{m=1 \\ m \neq n}}^{N} \big(- g_{n,m} \big) U_m = J_n. \tag{3.16}$$

This tells us the exact expression for the transfer matrix A relating $\mathbf{U}$ to $\mathbf{J}$, for the case of this web-like resistor grid. If we define

$$G_n = \sum_{m \neq n} g_{n,m} \tag{3.17}$$

we can write the transfer matrix A using these conductances, as

$$A = \begin{pmatrix} G_1 & -g_{1,2} & -g_{1,3} & \cdots & -g_{1,N} \\ -g_{2,1} & G_2 & -g_{2,3} & \cdots & -g_{2,N} \\ -g_{3,1} & -g_{3,2} & G_3 & \ddots & \vdots \\ \vdots & \vdots & \ddots & \ddots & -g_{N-1,N} \\ -g_{N,1} & -g_{N,2} & \cdots & -g_{N,N-1} & G_N \end{pmatrix} \tag{3.18}$$

The transfer matrix for such a web-like resistor grid is then simply $(-g_{n,m})$ in element (n, m) and (m, n), and positive main diagonal such that all rows sum to zero.

The inverse interpretation, as a matter of fact, is valid as well. Such transfer matrices always have positive main diagonals and negative off diagonals, with all

row sums zero [20]. For any transfer matrix A, then, its entries define a web-like resistor grid with identical behaviour to the system that it describes.

In case this attempted explanation has caused any confusion, it should be noted that this web-like resistor grid is not meant to serve as some strange discretization of Ω. Rather, it is intended here to illustrate that the entries of the matrix A are related to how well the surface nodes conduct current between one another.

Some algebraic properties of A now present themselves immediately, and are worth considering. First, A is symmetric, because $g_{n,m} = g_{m,n}$. Furthermore, A is weakly diagonally dominant, because its rows all sum up to zero, and as a result it is singular.

This fact, that A is not invertible, can be motivated from purely physical insight. Note that any uniform potential field placed on the surface nodes (i.e. all U_n having the same value) should not cause any current in the system, nor demand any from the outside. That is, the product of A with a single valued vector must equal the zero vector, which means its null-space is not empty.

The lack of an inverse A^{-1} might pose a problem. However, we can simplify our linear system, taking advantage of certain conservation laws and symmetries. It is possible to find an equivalent matrix of dimension $(N-1) \times (N-1)$ that is invertible, yet loses no functionality. This can be done in the following way:

Since the baseline of the potential is arbitrary, we can with impunity set one of the values U_n to 0, for instance U_N. The last column of A will then serve no purpose in equation (3.12), and can be ignored.

With respect to $\mathbf{J}$, since there are no sources of current inside the grid, the currents resulting from our measurements at the edge must sum up to zero. This fact allows us to discard one element J_n, for instance J_N, as we can always trust that it will be minus the sum of the other currents.

We must then also remove the corresponding row from A, turning A into an $(N-1) \times (N-1)$-matrix, which now *will* be invertible. Let us use the notation $A^\dagger$ to mean the inverse of this $(N-1) \times (N-1)$ matrix, with zeros reinserted afterwards in the removed row and column. Then,

$$\mathbf{U} = A^\dagger \mathbf{J}. \tag{3.19}$$

With this matrix, we can finally move on to relate A to the apparent resistivities ρ_a.

From a quadripole measurement of ρ_a, all of the vector $\mathbf{J}$ above is known. The external current into the ground is I at $C1$, $-I$ at $C2$, and zero at all other boundary nodes,

$$\mathbf{J} = (0, \ldots, 0, I, 0, \ldots, 0, -I, 0, \ldots, 0)^T \tag{3.20}$$

or in component form using the Kroenecker-delta,

$$J_n = I(\delta_{n,C1} - \delta_{n,C2}). \tag{3.21}$$

Thus equation (3.19) in component form becomes

$$\begin{aligned} U_m &= \sum_{n=1}^{N-1} A^\dagger_{m,n} J_n = \sum_{n=1}^{N-1} A^\dagger_{m,n} I(\delta_{n,C1} - \delta_{n,C2}) \\ &= I(A^\dagger_{m,C1} - A^\dagger_{m,C2}), \end{aligned}$$

While quadripole measurements do not give us the actual value of any of the elements in $\mathbf{U}$, they do tell us the potential difference V measured from $P1$ to $P2$. That gives us the result

$$V \;=\; U_{P1} - U_{P2} \;=\; I(A^{\dagger}_{P1,C1} - A^{\dagger}_{P1,C2} - A^{\dagger}_{P2,C1} + A^{\dagger}_{P2,C2})$$

so that the apparent resistivity ρ_a of the points $(C1, C2, P1, P2)$, given by equation (2.1)

$$\rho_a = k\frac{V}{I},$$

can be expressed in terms of the transfer matrix A as

$$\rho_a = k\left(A^{\dagger}_{P1,C1} - A^{\dagger}_{P1,C2} - A^{\dagger}_{P2,C1} + A^{\dagger}_{P2,C2}\right). \tag{3.22}$$

Because of how we defined $A^{\dagger}$ to have zeros reinserted in the removed rows and columns, the expression above applies also in the cases when any of the measurement points are the Nth node.

3.4 Discretization of Ω

For discrete measurement points on $\partial\Omega$, the discretization of Λ_σ went almost by itself. The transfer matrix A appeared as the discrete analogy of the transfer function as an immediate consequence of how potentials and currents are related. In a similar way, we will in this section find that the conducting body Ω also has a natural discretization, although not entirely as effortless as that seen in the section above.

As was stated in the opening chapter, the scope of this thesis is limited to the simpler, purely 2D inversion problem. It should therefore be noted that this simplification does limit the reach of our end discussion and conclusion to some extent. While real life ERT measurements are most often performed in order to generate a 2D-image, i.e. a cross section of the subsurface, the measurements themselves and their numerical treatment are fundamentally 3-dimensional in nature. Still, the investigation of the 2D problem can lead the way for further research, and the inversion problem is still based on the same physical laws and core concepts. Furthermore, the goal of this thesis is not to arrive at a final fully functioning program to rival RES2DINV, but to test these treacherous waters of the Calderón problem for the simulated annealing algorithm.

From this point on, the conducting body Ω will be regarded as 2-dimensional. It will be modelled as a grid of resistors, with edge nodes being our measurement points. Resistor network approximations arise quite naturally from finite volume discretizations of equation (3.3), where the law of conservation of currents turns into Kirchhoff's current law.

There has been much research dedicated to approximating the behaviour of conducting media by resistor grids. It has been shown that they can approximate the DtN-map with spectral accuracy, for a conducting body with known σ, simply

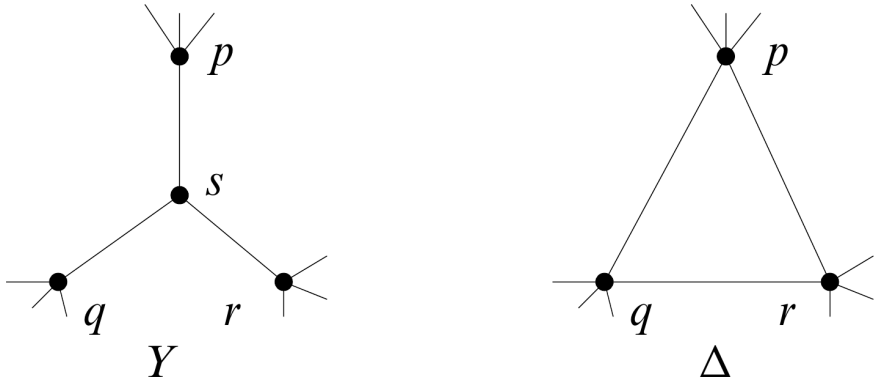

Figure 3.5: For an arbitrary choice of resistors in the Y-shaped network on the left, there is a Δ-shaped network like the one on the right that is indistinguishable for measurements at the nodes p, q, and r. Illustration taken from [4, p. 86].

by placing the nodes of the grid optimally [21]. These optimal node positions may be determined in different ways depending on the problem, for instance by advanced sensitivity analysis of the particular conductance function and grid in question, as described in [4, p. 88]. While all these results and methods are not necessary for us to simply use a resistor grid discretization, they do lend credence to this choice. The fact that the issue of node positions has been explored with such rigour also allows us to brush off that particular question for the moment. Such issues fall well outside the scope of this thesis.

A resistor grid is defined by its graph, denoted Γ, which describes its shape, and the conductances g_m of all its resistors, numbered $m = 1, \ldots, M$. The graph with which we decide to model Ω has to be chosen with care. First of all, it has to meet a certain criticality condition [4, p. 85] in order for all conductances to be at all recoverable from the transfer matrix A. It should also be noted that the graph Γ cannot be recovered from the transfer matrix A. This fact is often illustrated with the $Y - \Delta$ transformation, illustrated in figure 3.5. Any Y-shaped network will have a Δ-shaped network with indistinguishable behaviour at the nodes p, q, and r, and vice-versa.

The choice of Γ plays a key role in the solvability of our inverse problem, as making a bad choice may lead to the problem being indeterminable. For instance, the rectangular grid of figure 3.6a, perhaps the most obvious first choice of resistor grid, turns out not to be critical. Thus its conductances cannot all be recovered from its transfer matrix.

An easy way to see this is to consider one of the lower corners of the grid.

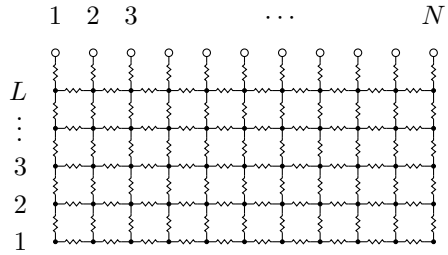

(a) Rectangular resistor grid, with boundary along top edge.

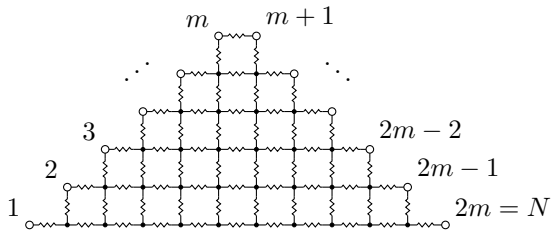

(b) Pyramidal resistor grid, with boundary marked by white nodes.

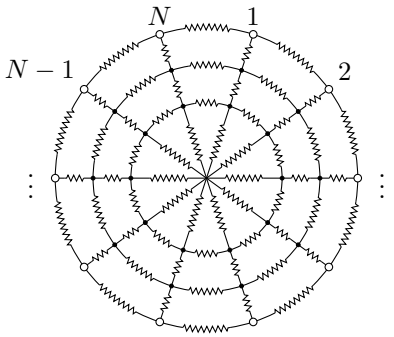

(c) Cirular resistor grid, with boundary marked by white nodes.

Figure 3.6: Three different resistor grids.

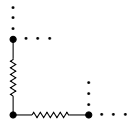

These two resistors can take on an infinite combination of conductances, so long as their combined effect is the same when measured from the two nodes connecting them to the rest of the grid. There are two degrees of freedom to be determined, but the only provide our measurements with one. Therefore, the rectangular grid of figure 3.6a is indeterminable.

One might think that this could be fixed by replacing these two resistors with just one, but unfortunately the problem goes deeper than this. If we look at a larger section of the corner, now consisting of six resistors,

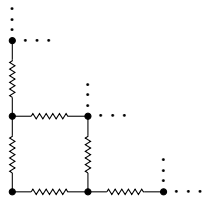

we see that they are connected to the rest of the grid at just three nodes. The resistors then have six combined degrees of freedom (or five if we replace the two outer ones), which can not all be determined from only three connections to the rest of the grid (the transfer matrix for the three nodes will be 3×3 containing only 3 independent elements, i.e. less than 6). This same argument can be applied to larger and larger corners for large rectangular grids, which only makes the problem worse.

The pyramidal resistor grid shown in figure 3.6b is known to be critical [22], but its shape is not flat like the ground of an ERT measurement. In order for this grid to be used, the optimal placement of the nodes will have to be determined by the advanced bethods alluded to earlier. Then, the grid nodes and resistors may be mapped onto the shape of the conducting body being modelled, but this is unnecessarily involved for our purposes.

While finding optimal node placements and an appropriate mapping of the grid shape may seem cumbersome, this grid does have some advantages to it. That is, exact algorithms have been found for this grid, and others like it, that will recover the precise conductance values of the grid from A, provided the transfer matrix is compatible. For details on this algorithm, see [4, pp. 97,98]. This compatibility of A is not always satisfied, however, and the algorithm is limited to this exact grid, for the strictly 2D problem, so the existence of such grids and algorithms do not nullify the effort of this thesis.

The resistor grid that may give us the best odds of successfully inverting surface measurements is the circular grid in figure 3.6c. With measurement points located on all sides of the grid, even the resistors deepest in its interior are relatively close

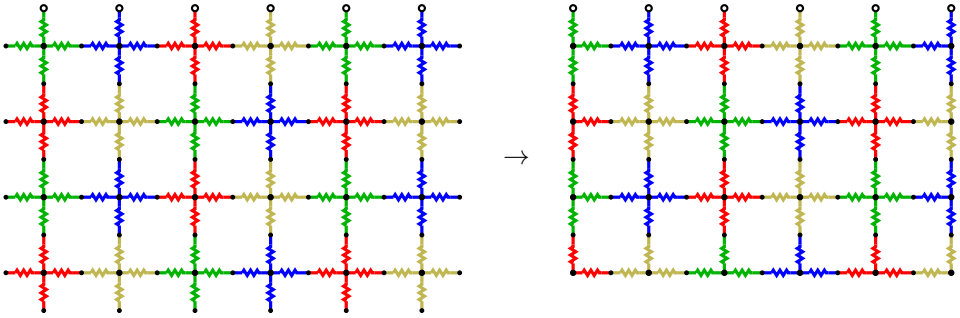

Figure 3.7: Illustration of how the conductance parameters may be distributed to the nodes of the grid instead of the resistors directly, using color codes to mark nodal relation. In the grid to the left all nodes show their four exiting half resistor, and to the right all loose resistors have been stripped away

to most of the surface nodes. But, while it may present the easiest target for our inversion scheme, the circular shape is too far removed from the situation of ERT in geophysical surveys.

Fortunately, there is a way to alter the rectangular grid so as to make it determinable by the transfer matrix. The necessary modification is analogous to the way RES2DINV divided up its subsurface model into blocks of uniform resistivity. In a similar way, the conductances of the grid can be distributed *at the grid nodes*, instead of the resistors directly, as illustrated in figure 3.7. The resistor between two nodes, labeled n and m, is then instead treated as consisting of two half-resistors in series, with combined conductance given by the two nodal conductances g_n and g_m as

$$g_{n,m} = \left(\frac{1}{g_n} + \frac{1}{g_m} \right)^{-1} = \frac{g_n g_m}{g_n + g_m}. \tag{3.23}$$

Figure 3.7 shows, with the help of colours, how we may think of each node as a kind of star, with four half-resistors of its particular conductance pointing out in all directions. At the edge nodes there will be some loose half-resistors, which we may remove as shown to the right in the figure. Note that the upper vertical half-resistors of the top layer are then not removed.

It is easy to check that this configuration will not fall victim to the same indeterminacy as did the regular rectangular grid, and the fact that RES2DINV discretizes the subsurface in a very similar way makes this seem like the best resistor grid for our purposes.

The dimensions of the resistor grid are also important in order for it to be determinable from the transfer matrix. The total number of parameters to be determined must not exceed the number of independent values in A, and because the matrix is symmetric with zero row sums, we will for N electrodes have $N(N-1)/2$ independant values in A. As a consequence, the depth of the grid, which we will

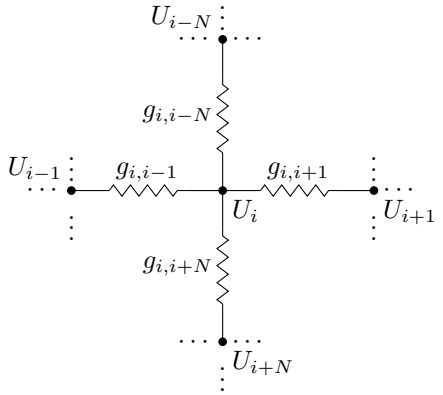

Figure 3.8: The junction with label i in a rectangular resistor grid, where four resistors connect it to the juntions $i-1$, $i+1$, $i-N$, $i+N$. Each junction, or node, has a potential, like U_i, and the conductance of the link between them is $g_{i,j}$, etc.

denote L, has to be small enough so that $\frac{N(N-1)}{2} \geq NL$, resulting in the condition

$$L \leq \frac{N-1}{2} \qquad \Leftrightarrow \qquad N \geq 2L+1 \tag{3.24}$$

for the rectangular grid with nodally distributed conductance.

With the graph of our grid decided, we are ready to move on to the laws determining its behaviour. As mentioned, the electrostratic equations of the continuous formulation discretize in a natural way on resistor grid. The fact that the current field is without sources inside of Ω implies that

$$\nabla \mathbf{J} = 0 \quad \Leftrightarrow \quad \oint \mathbf{J} \cdot \mathbf{dA} = 0 \tag{3.25}$$

which in words is to say that the total current out of any closed volume is zero. For resistor grids, this is precisely the same statement as Kirchhoff's current law.

Let the potential at node i of the grid be denoted U_i. Then, using figure 3.8 as reference, and by setting $g_{i,j} = 0$ for pairs of (i,j) that are not connected, we can express Kirchhoff's current law as follows:

$$\sum_{n \neq i} g_{i,n}(U_i - U_n) \; = \; 0. \tag{3.26}$$

This is quite similar to what we did in the previous section with the web-like resistor grid, so what follows should not come as a surprise. Rearranging, we see that the above can be written as a matrix product

$$\left(\sum_{n \neq i} g_{i,n} \right) U_i \; + \; \sum_{n \neq i} (-g_{i,n}) U_n \; = \; 0 \tag{3.27}$$

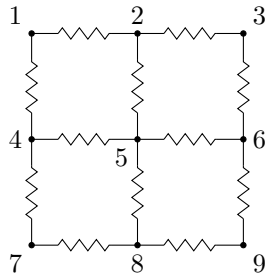

Figure 3.9: A 3-by-3 resistor grid

where the vector $\mathbf{U}$ now contains the potentials U_i for all internal nodes i.

If we denote the matrix defined by equation (3.27) as K, we may write

$$K\mathbf{U} = \mathbf{0} \tag{3.28}$$

which in fact is the resistor grid equivalent of equation (3.3),

$$\nabla \cdot \sigma \nabla u = 0.$$

Incidentally, the type of matrix K that comes out of such grids is referred to as Kirchhoff matrices. As an example to illustrate their structure, consider the resistor grid in figure 3.9. This grid, assuming 1Ω resistors, i.e. $g_{n,m} = 1\text{S}$ conductance in all, will have a Kirchhoff matrix by

$$K = \begin{pmatrix} 2 & -1 & & -1 & & & & & \\ -1 & 3 & -1 & & -1 & & & & \\ & -1 & 2 & & & -1 & & & \\ -1 & & & 3 & -1 & & -1 & & \\ & -1 & & -1 & 4 & -1 & & -1 & \\ & & -1 & & -1 & 3 & & & -1 \\ & & & -1 & & & 2 & -1 & \\ & & & & -1 & & -1 & 3 & -1 \\ & & & & & -1 & & -1 & 2 \end{pmatrix} \tag{3.29}$$

in which open spaces denote elements equal to 0.

Note that K can be thought of as the transfer matrix of the entire grid simultaneously, internal and external nodes all included. Equation (3.28) then simply states that whatever the potential at each node may be, the sum of currents flowing into and out of each node of the grid must be zero. Or phrased in a different way, there should be no *external* sources of current.

If there were any external currents present, for instance as illustrated in the middle of figure 3.10, the zero vector on the right would instead become the vector of external currents into each of the nodes of the grid, that is,

$$K\mathbf{U} = \mathbf{J}. \tag{3.30}$$

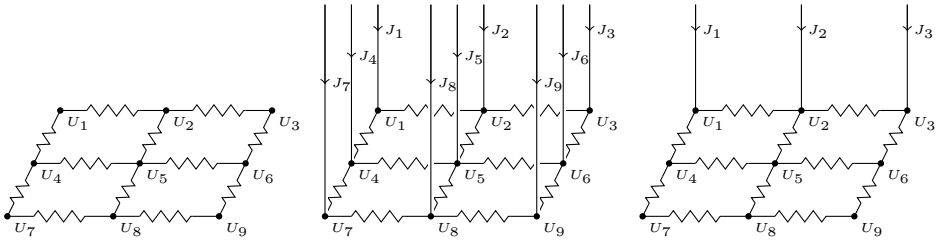

Figure 3.10: Illustration of three different situations for a grid of resistors with 9 nodes, electric potentials U_n, and external currents J_m applied either nowhere, everywhere, or at the boundary $\mathscr{B} = \{1, 2, 3\}$

In a surface measurement, a boundary condition is placed across the surface nodes, and so there will at those specific nodes be a current flowing into the grid. Yet the internal nodes i still obey equation (3.27), so those elements in $\mathbf{J}$ can be set to zero. In order to make clearer the distinction between interior and border nodes, we can consider the Kirchhoff matrix as made up of four submatrices,

$$K = \begin{pmatrix} K_{\mathscr{B}\mathscr{B}} & K_{\mathscr{B}\mathscr{I}} \\ K_{\mathscr{I}\mathscr{B}} & K_{\mathscr{I}\mathscr{I}} \end{pmatrix}, \tag{3.31}$$

in which, for the grid considered earlier, and $\mathscr{B} = \{1, 2, 3\}, \mathscr{I} = \{4, \ldots, 9\}$,

$$K_{\mathscr{B}\mathscr{B}} = \begin{pmatrix} 2 & -1 & \\ -1 & 3 & -1 \\ & -1 & 2 \end{pmatrix}, \qquad K_{\mathscr{B}\mathscr{I}} = \begin{pmatrix} -1 & & & & & \\ & -1 & & & & \\ & & -1 & & & \end{pmatrix},$$

$$K_{\mathscr{I}\mathscr{B}} = \begin{pmatrix} -1 & & \\ & -1 & \\ & & -1 \\ & & \\ & & \\ & & \end{pmatrix}, \qquad K_{\mathscr{I}\mathscr{I}} = \begin{pmatrix} 3 & -1 & & -1 & & \\ -1 & 4 & -1 & & -1 & \\ & -1 & 3 & & & -1 \\ -1 & & & 2 & -1 & \\ & -1 & & -1 & 3 & -1 \\ & & -1 & & -1 & 2 \end{pmatrix},$$

and similarly for $\mathbf{U}$ and $\mathbf{J}$,

$$\mathbf{U} = \begin{pmatrix} \mathbf{U}_{\mathscr{B}} \\ \mathbf{U}_{\mathscr{I}} \end{pmatrix}, \qquad \mathbf{J} = \begin{pmatrix} \mathbf{J}_{\mathscr{B}} \\ \mathbf{J}_{\mathscr{I}} \end{pmatrix}.$$

The subscripts indicate which rows and columns belong to which nodes in the grid; The set of border nodes is marked by $\mathscr{B}$ and the set of interior nodes by $\mathscr{I}$. With this sorting of nodes in mind, we can rewrite equation (3.30) as

$$\begin{pmatrix} K_{\mathscr{B}\mathscr{B}} & K_{\mathscr{B}\mathscr{I}} \\ K_{\mathscr{I}\mathscr{B}} & K_{\mathscr{I}\mathscr{I}} \end{pmatrix} \begin{pmatrix} \mathbf{U}_{\mathscr{B}} \\ \mathbf{U}_{\mathscr{I}} \end{pmatrix} = \begin{pmatrix} \mathbf{J}_{\mathscr{B}} \\ \mathbf{J}_{\mathscr{I}} \end{pmatrix}. \tag{3.32}$$

But as mentioned, for measurements at the surface nodes of a grid we know that there are no external currents directed into the internal nodes. Then we have that $\mathbf{J}_{\mathscr{I}} = \mathbf{0}$, resulting in the important equation

$$\begin{pmatrix} K_{\mathscr{B}\mathscr{B}} & K_{\mathscr{B}\mathscr{I}} \\ K_{\mathscr{I}\mathscr{B}} & K_{\mathscr{I}\mathscr{I}} \end{pmatrix} \begin{pmatrix} \mathbf{U}_{\mathscr{B}} \\ \mathbf{U}_{\mathscr{I}} \end{pmatrix} = \begin{pmatrix} \mathbf{J}_{\mathscr{B}} \\ \mathbf{0} \end{pmatrix}. \tag{3.33}$$

The situations described by equations (3.28), (3.32), and (3.33) are all illustrated in figure 3.10.

The importance of equation (3.33) is hard to overstate in this discretized model. First of all, it gives us an expression for the transfer matrix A of the grid. Inserting the bottom row of the block expression into the top row, we get

$$K_{\mathscr{I}\mathscr{I}}\mathbf{U}_{\mathscr{I}} \;=\; -K_{\mathscr{I}\mathscr{B}}\mathbf{U}_{\mathscr{B}} \tag{3.34}$$

$$\Rightarrow \big(K_{\mathscr{B}\mathscr{B}} - K_{\mathscr{B}\mathscr{I}}K_{\mathscr{I}\mathscr{I}}^{-1}K_{\mathscr{I}\mathscr{B}}\big)\mathbf{U}_{\mathscr{B}} \;=\; \mathbf{J}_{\mathscr{B}} \tag{3.35}$$

where A has magically[2] appeared as

$$A \;=\; K_{\mathscr{B}\mathscr{B}} - K_{\mathscr{B}\mathscr{I}}K_{\mathscr{I}\mathscr{I}}^{-1}K_{\mathscr{I}\mathscr{B}} \tag{3.36}$$

We see above that the transfer matrix A, which completely determines the outcome of any surface measurements, can be found knowing the grid structure and resistor strengths. This fact in and of itself is not shocking, but the expression for A above is rather elegant. But that is not all.

Equation (3.33) is in fact the discrete equivalent of equation (3.3), yet simultaneously encodes *both* kinds of boundary conditions discussed in the continuous formulation. Starting from nothing more than Kirchhoffs laws, we have an equation that serves triple duty, becoming *the* governing equation for potentials and currents in resistor grids.

If we know K, or the grid structure as given by $(\Gamma, \{g_{n,m}\})$, equation (3.33) uniquely determines the potential at interior points once we fix either the boundary potentials or currents. Proving this requires no effort; we may simply write down the answer from (3.34):

$$\mathbf{U}_{\mathscr{I}} \;=\; \begin{cases} -K_{\mathscr{I}\mathscr{I}}^{-1}K_{\mathscr{I}\mathscr{B}}\mathbf{U}_{\mathscr{B}}, & \text{for fixed surface potentials,} \\ -K_{\mathscr{I}\mathscr{I}}^{-1}K_{\mathscr{I}\mathscr{B}}A^{\dagger}\mathbf{J}_{\mathscr{B}}, & \text{for fixed surface currents.} \end{cases} \tag{3.37}$$

In case this matrix formulation has hidden the weight that these equations carry, it might be worth rephrasing them in clearer terms. Equation (3.33) is nothing more than Kirchhoff's first and second laws in matrix form. These laws are the discrete equivalent of $\nabla \cdot \sigma \nabla u = 0$. By simply writing them in this more compact

[2] As an aside, we see here that the transfer matrix A of a resistor grid can be described algebraically as the Schur complement of K with respect to its submatrix $K_{\mathscr{I}\mathscr{I}}$, often written simply as $A = K/K_{\mathscr{I}\mathscr{I}}$. This is a specific case of a more general result; If we want to find the transfer matrix for measurements at a specific subset of nodes, we can do so by taking the Schur complement of K with respect to the submatrix of rows and columns belonging to excluded nodes. [20]

way, discrete analogies to all the concepts involved in the continuous description seem to just come falling out on their own. There is a comforting consistency in the way we discretized the problem.

Because the discrete picture corresponds so well with the continuous one at the start of the chapter, the discrete version of the inverse problem almost writes itself. In Calderón's continuous formulation, the relevant objects were the conductivity σ, the conducting body Ω, and the transfer function Λ_σ. Here, these are replaced by the conductivities $g_{n,m}$ of the grid resistors, the graph Γ of the resistor grid, and the transfer matrix A;

> Recover the conductivities g_i of a resistor grid with graph Γ, from its transfer matrix A.

The forward problem, meanwhile, can be phrased as finding A for a given resistor grid. But we already know the solution to this, as it is given by equation (3.36). However, while that expression will give the correct values in A, it does not present us with a particularly efficient algorithm for actually computing the transfer matrix. For larger grids, where the size of $K_{\mathscr{I}\mathscr{I}}$ becomes huge, the expression quickly becomes extremely computationally expensive. In the next chapter we shall see that there are methods of computing A that are more efficient.

Chapter 4

The forward problem

In the previous chapter we discretized the continuous conducting region Ω with conductivity σ, as a resistor grid with graph Γ and conductances $g_{n,m}$. The continuous electrostatic equations then became Kirchhoff's circuit laws, which could be written compactly using the Kirchhoff matrix K

We found that by writing K in terms of four submatrices, of rows and collumns belonging to either boundary or interior nodes,

$$K = \begin{pmatrix} K_{\mathscr{B}\mathscr{B}} & K_{\mathscr{B}\mathscr{I}} \\ K_{\mathscr{I}\mathscr{B}} & K_{\mathscr{I}\mathscr{I}} \end{pmatrix}$$

we could write down an expression for the transfer matrix A of the grid,

$$A \;=\; K_{\mathscr{B}\mathscr{B}} - K_{\mathscr{B}\mathscr{I}} K_{\mathscr{I}\mathscr{I}}^{-1} K_{\mathscr{I}\mathscr{B}} \tag{4.1}$$

being the solution to the discrete forward problem. But the expression above is unwieldy, and in general not at all conducive to rapid computation. In this chapter we will describe a scheme to more quickly compute the transfer matrix A for a range of resistor grids, first introduced by Derrida-Vannimenus in 1982 [23].

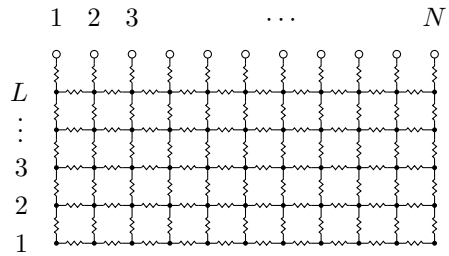

Figure 4.1: A rectangular grid, with measurement nodes at the top edge marked as white, for which we want to efficiently compute the transfer matrix A.

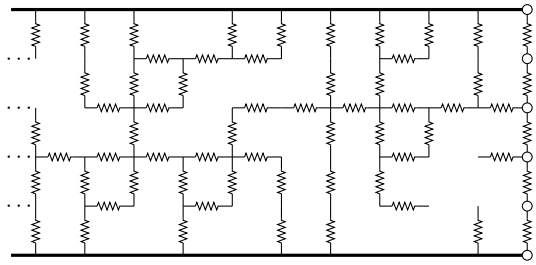

Figure 4.2: Illustration of the porous conducting medium considered by Derrida and Vannimenus, in a mix of 1Ω and infinite resistors determined by a probability p, in this case $p = 2/3$. The nodes described by the transfer matrix A are indicated with white circles.

4.1 Rectangular grid

In their paper [23], Derrida and Vannimenus considered rectangular bands of porous conducting media. They were investigating percolation properties of conductive materials, by letting the individual resistances be either 1Ω or infinite with some proportion. In their model, illustrated in figure 4.2, the grid was sandwiched between two metal plates, modeled as having zero resistivity, and a transfer matrix described the response of one of the two side edges.

Derrida and Vannimenus derived an algorithm for updating the transfer matrix A as they built onto the edge of this resistor network, placing 0Ω resistors to model metal plates, and either 1Ω or infinite resistors inside the grid with probabilities p and $(p-1)$. Their algorithm allowed them to grow their porous conducting band arbitrarily long, all the while having an updated and correct transfer matrix for the resistor grid. After using this algorithm for a very large random resistor network, they could read off the combined conductivity of the porous medium from one metal plate to the other, by using the final values in the transfer matrix A. Doing this for a range of probabilities p and band widths, they were able to characterize the percolation properties of the system.

While our model does not place the resistor grid between two metal plates, nor do we require our grid depth to be arbitrarily deep, their derivation can with few modifications be used to give us a quite efficient scheme for computing our transfer matrices as well. The algorithm even does so *exactly*.

Our starting point is a single layer of resistors, as seen in figure 4.3. All resistors are between nearest neighbour nodes, and we may denote the conductance between node n and $n+1$ by $g_{n,n+1}$. Finding A for such a "grid" is trivial, given what we know from the previous chapter. The resulting matrix is tridiagonal, and can be written down as

$$A = \begin{pmatrix} g_{1,2} & -g_{1,2} & & & \\ -g_{1,2} & g_{1,2}+g_{2,3} & -g_{2,3} & & \\ & \ddots & \ddots & \ddots & \\ & & -g_{N-1,N} & g_{N-1,N} \end{pmatrix}, \tag{4.2}$$

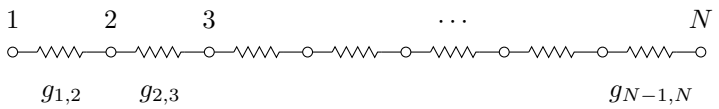

Figure 4.3: A resistor "grid", consisting of a single layer of resistors, conductances $g_{n,n+1}$ labeled.

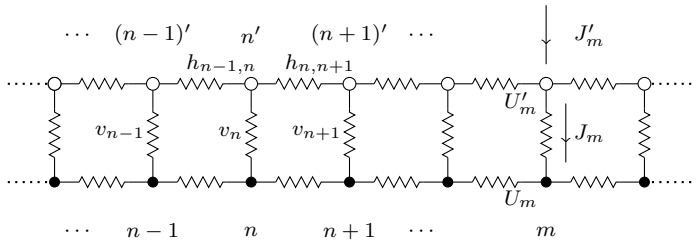

Figure 4.4: The second layer of a resistor grid, added on top of the first seen in figure 4.3. Labels are included to show the position of horizontal and vertical resistors at node n, with conductance h_n and $v_{n,n\pm1}$, and the currents and potentials into node m and m'.

where we note that all row-sums are zero, as they should be.

From this starting point, we may consider what happens as we add a second layer of resistors onto our one-layer "grid", as indicated in figure 4.4. To emphasize the difference between *vertical* and *horizontal* resistors[1], the vertical resistor at node n has conductance denoted by v_n, while the horizontal resistor from n to $n+1$ has conductance $h_{n,n+1}$. The goal now is to find a matrix A', expressed in terms of the old A and these new resistors, satisfying

$$A'\mathbf{U}' = \mathbf{J}' \tag{4.3}$$

for the new surface potential and current vectors $\mathbf{U}'$ and $\mathbf{J}'$.

Let us denote by U_n the potential at the previous nth node, and U'_n the potential at the new layer n'th node. Then the current running down through the nth vertical resistor to node n must be given by $J_n = v_n(U'_n - U_n)$. By defining the diagonal

[1]It should be noted that our concepts of "vertical" and "horizontal" are the opposite compared to those of Derrida and Vannimenus. They imagined building on the grid sideways, with the metal plates sandwiching the resistor grid from above and below. This leads to a mix up in notation, but the meaning remains the same.

matrix V with nth diagonal element v_n,

$$V \equiv \begin{pmatrix} v_1 & & \\ & \ddots & \\ & & v_N \end{pmatrix} \tag{4.4}$$

this can be written as a matrix product by

$$\mathbf{J} = V(\mathbf{U}' - \mathbf{U}).$$

But we know already that the bottom layer needs a current $\mathbf{J} = A\mathbf{U}$ to support the potential vector $\mathbf{U}$. Therefore, we can write the above as[2]

$$(V + A)\,\mathbf{U} \;=\; V\,\mathbf{U}' \qquad \Rightarrow \qquad \mathbf{U} \;=\; (1 + V^{-1}A)^{-1}\,\mathbf{U}' \tag{4.5}$$

where 1 denotes the N-by-N identity matrix.

This relation between $\mathbf{U}$ and $\mathbf{U}'$ is the first step to finding A. The next is to express the new n'th boundary current J'_n in terms of the potentials surrounding it. Kirchhoff's current law grants us this, stating that

$$J'_n \;=\; h_{n,n+1}(U'_n - U'_{n+1}) \;+\; h_{n-1,n}(U'_n - U'_{n-1}) \;+\; J_n$$

which can be rearranged to give, for n not equal to 1 or N,

$$J'_n \;=\; -\,h_{n,n+1}U'_{n+1} \;+\; (h_{n-1,n} + h_{n,n+1})U'_n \;-\; h_{n-1,n}U'_{n-1} \;+\; J_n.$$

The cases when $n = 1, N$ simply lose the $h_{n-1,n}$ or $h_{n,n+1}$ terms. The above can be written as a matrix expression, by defining the tridiagonal matrix H

$$H \equiv \begin{pmatrix} h_{1,2} & -h_{1,2} & & \\ -h_{1,2} & h_{1,2} + h_{2,3} & -h_{2,3} & \\ & \ddots & \ddots & \ddots \\ & & -h_{N-1,N} & h_{N-1,N} \end{pmatrix}, \tag{4.6}$$

so that

$$\mathbf{J}' \;=\; H\mathbf{U}' + \mathbf{J}$$

This, along with $A\mathbf{U} = \mathbf{J}$ and equation (4.5), tells us that

$$\left(H + A(1 + V^{-1}A)^{-1}\right)\mathbf{U}' \;=\; \mathbf{J}'$$

from which it is plain to see that the matrix A' of equation (4.3) has to be the expression inside the parenthesis on the left above.

$$A' \;=\; H + A(1 + V^{-1}A)^{-1} \tag{4.7}$$

This is the matrix expression that lets us incrementally compute A for rectangular grids. It will obviously be exactly the same for the 3rd, 4th, etc. layers, and it is far more efficient than a naïv implementation of equation (4.1).

[2]Note that $(V + A)$ is certainly invertible, since A is weakly diagonally dominant, so that adding it to V will result in a strictly diagonally dominant matrix. The result then follows from rewriting $(V + A)^{-1}V = (1 + V^{-1}A)^{-1}$.

$$A = \begin{pmatrix} 1 & -1 & 0 \\ -1 & 2 & -1 \\ 0 & -1 & 1 \end{pmatrix}$$

$$A' = \begin{pmatrix} 1 & -1 & 0 \\ -1 & 2 & -1 \\ 0 & -1 & 1 \end{pmatrix} + \begin{pmatrix} 1 & -1 & 0 \\ -1 & 2 & -1 \\ 0 & -1 & 1 \end{pmatrix} \begin{pmatrix} 2 & -1 & 0 \\ -1 & 3 & -1 \\ 0 & -1 & 2 \end{pmatrix}^{-1}$$

$$= \begin{pmatrix} 1.375 & -1.25 & -0.125 \\ -1.25 & 2.5 & -1.25 \\ -0.125 & -1.25 & 1.375 \end{pmatrix}$$

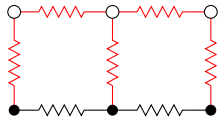

$$A'' = \begin{pmatrix} 1 & -1 & 0 \\ -1 & 2 & -1 \\ 0 & -1 & 1 \end{pmatrix} + \begin{pmatrix} 1.375 & -1.25 & -0.125 \\ -1.25 & 2.5 & -1.25 \\ -0.125 & -1.25 & 1.375 \end{pmatrix} \begin{pmatrix} 2.375 & -1.25 & -0.125 \\ -1.25 & 3.5 & -1.25 \\ -0.125 & -1.25 & 2.375 \end{pmatrix}^{-1}$$

$$= \begin{pmatrix} 1.432 & -1.263 & -0.168 \\ -1.263 & 2.526 & -1.263 \\ -0.168 & -1.263 & 1.432 \end{pmatrix}$$

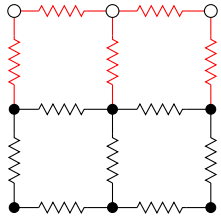

Figure 4.5: The transfer matrix of a small resistor grid, built up layer by layer.

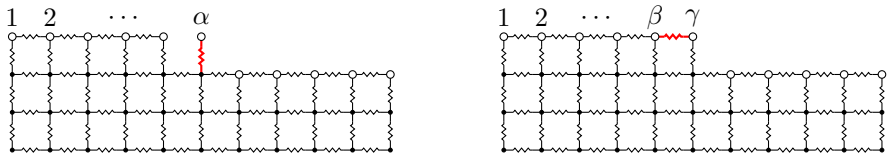

Figure 4.6: Building up the resistor grid resistor by resistor, vertical at α to the left, and horizontal from β to γ to the right.

In order to see this algorithm in practice, consider again the 3-by-3 resistor grid of 1Ω resistance, or 1S conductance. It is built up layer by layer in figure 4.5, where the computed matrices A,A', and A'' are shown for each layer. The final transfer matrix of the 3-by-3 grid, for measurements at the top edge nodes, is found to be

$$A = \begin{pmatrix} 1.432 & -1.263 & -0.168 \\ -1.263 & 2.526 & -1.263 \\ -0.168 & -1.263 & 1.432 \end{pmatrix}$$

As a consistency check, we can compute A for this small grid by equation (4.1),

$$\begin{aligned} A &= K_{\mathscr{B}\mathscr{B}} - K_{\mathscr{B}\mathscr{I}} K_{\mathscr{I}\mathscr{I}}^{-1} K_{\mathscr{I}\mathscr{B}} \\ &= \begin{pmatrix} 2 & -1 & \\ -1 & 3 & -1 \\ & -1 & 2 \end{pmatrix} - \begin{pmatrix} -1 & & \\ & -1 & \\ & & -1 \end{pmatrix} \begin{pmatrix} 3 & -1 & & -1 & & \\ -1 & 4 & -1 & & -1 & \\ & -1 & 3 & & & -1 \\ -1 & & & 2 & -1 & \\ & -1 & & -1 & 3 & -1 \\ & & -1 & & -1 & 2 \end{pmatrix}^{-1} \begin{pmatrix} -1 & & \\ & -1 & \\ & & -1 \\ & & \\ & & \\ & & \end{pmatrix} \\ &= \begin{pmatrix} 1.432 & -1.263 & -0.168 \\ -1.263 & 2.526 & -1.263 \\ -0.168 & -1.263 & 1.432 \end{pmatrix} \end{aligned}$$

giving exactly the same result, as expected.

For the grid in figure 4.1, which has the same top layer of vertical resistors as a rectangular grid with nodal conductance, it is more useful to phrase addition of horizontal resistors seperately from the vertical ones. Constructing A can then be done simply by L repetitions of adding "*horizontal layer, then vertical layer*", instead of modifying the current scheme of "*vertical layer, then horizontal layer*".

The resulting procedure follows from equation (4.7), by setting either horizontal or vertical conductances to zero or infinity respectively:

$$A' = A + H \qquad \text{horizontal resistor layer} \qquad (4.8a)$$

$$A'' = A'(1 + V^{-1}A')^{-1} \qquad \text{vertical resistor layer} \qquad (4.8b)$$

Equation (4.7) computes the altered A after adding one whole row of vertical and horizontal resistors simultaneously. In a later publication [18], Derrida et al.

provided expressions for adding single resistors of conductance g, both vertical and horizontal, as illustrated in figure 4.6.

$$\text{Vertical, at } \alpha: \qquad A'_{i,j} = A_{i,j} - \frac{A_{i,\alpha}A_{\alpha,j}}{g + A_{\alpha,\alpha}} \tag{4.9a}$$

$$\text{Horizontal, } \beta \text{ to } \gamma: \qquad A'_{i,j} = A_{i,j} + g(\delta_{i,\beta} - \delta_{i,\gamma})(\delta_{j,\beta} - \delta_{j,\gamma}) \tag{4.9b}$$

Note that the horizontal expression is a compact way of phrasing an addition of g to $A_{\beta,\beta}$ and $A_{\gamma,\gamma}$, and subtraction of g from $A_{\gamma,\beta}$ and $A_{\beta,\gamma}$. In their paper, the value of g was either 1 or 0, which greatly simplified the resistor-wise expressions and made them preferable to the full matrix equation in (4.7). A derivation for both the resistor-wise expressions above is provided in Appendix B.

4.2 Pseudocode

The incremental computation of A derived in the previous section easily lends itself to be expressed programmatically. This is seen in figure 4.7, in which the matrix approach has been taken in the case of the vertical resistors. The function described in the pseudocode requires the dimensions N and L of the resistor grid, as well as the horizontal and vertical resistor conductances in separate arrays g_h and g_v.

Recall from the previous chapter that rectangular resistor grids are not critical, and therefore cannot be recovered from their transfer matrix. A proposed solution to this problem was to instead attribute conductance values to the *nodes* of the resistor grid, computing the resistor values as if from two resistors in series. However, to implement this we require a way to translate the list of nodal conductances into horizontal and vertical conductances. This is done by the algorithm described in figure 4.8.

It can be seen both from the layerwise expressions in (4.8) and the resistorwise expressions in (4.9), that the time complexity for altering A with respect to one new layer is $\mathcal{O}(N^3)$. It is the vertical resistors that are eating up most of the time; they require the solution of a matrix equation in the layered approach (4.8b), and each of the N vertical resistors alter all of A in (4.8b).

The time complexity for computing A for a whole grid is then $\mathcal{O}(N^3L)$, or, because L will be proportional to N, of the order $\mathcal{O}(N^4)$. This has the potential of becoming a problem for large resistor grids, as our inversion algorithm will require computing A many, many times.

```
 1: function TransMat(N, L, g_h, g_v)
 2:     Let A be zero N × N matrices
 3:     Let g be a real number
 4:     Let n, l be integers
 5:     for l = 1 to L do
 6:         for n = 1 to N − 1 do                                  ▷ Horizontal
 7:             g ← g_h[l + 1, n]
 8:             A[n, n] ← A[n, n] + g
 9:             A[n, n + 1] ← A[n, n + 1] − g
10:             A[n + 1, n] ← A[n + 1, n] − g
11:             A[n + 1, n + 1] ← A[n + 1, n + 1] + g
12:         end for
13:         A ← A · ( 1 + diag(1/g_v[l, :])A )^{−1}                ▷ Vertical
14:     end for
15:     return A
16: end function
```

Figure 4.7: Compute the transfer matrix A, given the grid dimensions N and L, as well as the horizontal resistors in an $L \times (N-1)$ array g_h, and the vertical resistors in an $L \times N$ array g_v. The diag-function constructs a sparse diagonal $N \times N$ matrix from a list of N numbers. The matrix expression in line 13 is readily handled by most linear algebra libraries.

```
1: function SERIES(g_1, g_2)                          ▷ Help function, resistors in series
2:     return g_1 g_2/(g_1 + g_2)
3: end function
4:
5: function SPLITG(N, L, g)
6:     Let g_h be a L × (N − 1) array
7:     Let g_v be a (L − 1) × N array
8:     Let n, l be integers
9:     for l = 1 to L do                                          ▷ Horizontal resistors
10:        for n = 1 to N − 1 do
11:            g_h[l, n] ← SERIES(g[Nl + n], g[Nl + n + 1])
12:        end for
13:    end for
14:    for l = 1 to L do                                          ▷ Vertical resistors
15:        for n = 1 to N do
16:            g_v[l, n] ← SERIES(g[Nl + n], g[N(l + 1) + n])
17:        end for
18:    end for
19:    return g_h, g_v
20: end function
```

Figure 4.8: Find the horizontal and vertical resistor conductances g_h and g_v of a $N \times L$ grid, from a list g of length (NL) of nodal conductivities. The nodes are assumed to be numbered 1 to NL, from bottom row to top in g. These arrays g_h and g_v can be used in the computation of the transfer matrix A. A help function "SERIES" is used for computing the conductance of two resistors in series.

Chapter 5

Minimisation

Thus far, we have become familiar with the practical application of ERT, studied the formal description of the inverse problem at hand, and found an algorithmic way to solve the forward problem. This chapter will go on to describe the algorithm with which we hope to solve the Calderón problem numerically, namely the method of *simulated annealing* (SA).

Inverse problems can in general be classified as ill-posed, making them usually very difficult to solve numerically. They tend to have unstable, or sometimes even degenerate solutions, with a highly irregularly shaped solution space [24, p. 7]. In this sense the Calderón problem is typical, as it is indeed severely ill-posed.

The Calderón problem can generally be phrased as finding a model with behaviour or response similar to an unknown measured system. We will phrase this as a minimisation problem, to minimise the error between a set of measurements and the response of our model resistor grid, with the hopes that this will lead us to the right inverted image.

Other approaches, for instance the one used by Loke in RES2DINV, also attempt to minimise the error between measurements and model respons. However, in the case of Loke, the chosen algorithm is based on local optimisation, and therefore rely on regularising the objective function. This is done in RES2DINV by defining the minimisation in terms of specific apparent resistivities, from specific quadripole arrays, sensitive to specific kinds of behaviour in the ground.

While the ill-posedness of our problem may have been mentioned multiple times already, it bears repeating at the beginning of this chapter. The central proposition of this thesis is that the minimisation algorithm should be chosen to fit the problem itself. As is explained in this chapter, simulated annealing is in that sense an algorithm worth serious consideration in the context of the Calderón problem, because of its many properties and history of success with highly challenging and ill-posed problems. The algorithm will be described, with all of its several components, before the detailed implementation of this thesis is put forth.

5.1 Simulated annealing

In general, the method of simulated annealing (SA) is an algorithm for finding the global minimum of an objective function, which we will denote E. The algorithm is applicable to a huge range of problems, as the domain of E can be virtually of any kind, from permutations of a set and other kinds of discrete configuration spaces, to a vector of n continuous variables in $\mathbb{R}^n$.

It particularly shines in the context of difficult combinatorial problems. Sometimes described as "nature's own minimisation algorithm", it is said to have practically "solved" the travelling salesman problem [25]. But its practicality is not limited to discrete problems, as it has been used to successfully solve a wide range of difficult problems with continuous parameters as well [26].

The method draws inspiration from statistical mechanics, in an analogy with physical systems that have a unique but well hidden ground state at which the energy is minimal. A physical analogy will be most helpful to illustrate its core ideas:

Consider a red hot rod of iron. On the atomic level, the high temperature gives rise to chaotic behaviour, and a lack of any fixed structure in the metal. The atoms are not bonded in a rigid lattice, and so they are free to shift relative to one other, making the red hot iron very flexible.

Now imagine cooling the iron. If the cooling process is gradual enough, over a sufficiently long stretch of time, the atoms will slowly shift and settle down into a very stable lattice structure, bonding together nicely with their neighbours. In the end, the atoms in the metal have found a configuration of very low energy, and the result is a strong iron rod.

Now imagine instead rapidly cooling the iron, for instance by dropping it in a bucket of cold water. The atoms quickly lose the energy they previously had to move around, so quickly that they do not have time to gradually find the same optimal configuration as in the case of gradual cooling. If cooled in this rapid manner instead, the atoms of the iron rod do not end up in a low energy configuration, and as a result the rod will be brittle rather than strong.

The slow and gradual cooling of a metal, as in the first description, is known as *annealing*, whereas the other shock-like way of cooling metal is referred to as *tempering*. It is from this analogy with cooling metals that the algorithm also gets its name. The input of the objective function E is treated as the configuration of a physical system, like the movements and relative positions of each atom in the iron rod, and the value of E plays the role of the system energy. Then, to make the analogy complete, a control parameter T is introduced, playing the role of temperature.

In essence, the algorithm gradually lowers the temperature T, while repeatedly changing the parameters of E in a "random walk"-like fashion between each lowering. The random walk is biased towards lower values of E, by always accepting a step down in energy, but also sometimes accepting a step up to higher energy. Specifically,

an acceptance probability p, given by

$$p = \min\left(1,\ \exp\left(-\frac{E_2 - E_1}{kT}\right)\right) \tag{5.1}$$

is used, for accepting a new step with energy E_2 from a configuration of energy E_1. Above, k is a constant analogous to the Boltzmann constant k_B. In the next section this expression will be properly motivated from the standpoint of statistical mechanics.

The hope is that constantly altering the system in this way will keep its configuration in the range of permitted states for the current temperature, even as T gets lowered. If this is ensured while T approaches zero, the system will converge to the *global minimum* of E.

By contrast, most minimisation algorithms are more easily compared to the tempering of metal. The goal is usually to find a lower value of E as quickly and in as few steps as possible, which in many situations is entirely sufficient. But for systems of more complex and irregular behaviour, this greedy approach is at risk of instead ending up in a non-optimal local minimum of E, in the same way that the atoms of the metal rod were tempered into a high energy configuration.

These properties of SA would seem to make it the perfect algorithm for numerically solving difficult inverse problems. It elegantly circumvents the difficulties posed by ill-posedness, by taking its time to patiently coax the system into the global minimum. There are many examples of SA applied to a wide range of inverse problem, like the "Patient Zero"-inverse problem [5], or the design of solar collectors [6]. Even within the field of geophysics, it has been used to locate interfaces in layered media [7], invert the acoustic response of 2D inhomogeneous media, and, in an application particularly closely related to this thesis, to invert data from the electromagnetic prospecting technique "mise-à-la-masse" [8]. This well documented success of SA is another reason to be optimistic of our strategy.

With some intuitive understanding now under our belt, let us move on to a more precise description of the SA algorithm. As explained in [25], it requires four components in order to be used:

1. The *objective function* E itself, to be minimised.
2. A *description of the possible system configuration*, or the domain of E.
3. A *generator of random changes in the configuration*, which presents the algorithm with suggested steps in the random walk.
4. An *annealing schedule*, to dictate how and when the control parameter T is to be lowered.

With these, an SA algorithm can be implemented, a general outline for which is presented in figure 5.1. We will in this chapter go through each of these four required components in more detail, and argue for the implementation that has been chosen in our numerical experiments. But first, to fascilitate the discussions to come, it will be useful to start with a review of the relevant concepts from statistical mechanics.

```
1: function SimAnneal(E, T_end, n_end)
2:     Let x_1, x_2, x_min be chosen randomly from the domain of E
3:     Let E_1, E_2, E_min, T be real numbers
4:     Let n be an integer
5:
6:     E_1 ← E(x_1)
7:     E_2 ← E(x_2)
8:     E_min, x_min ← lowest energy((E_1, x_1), (E_2, x_2))
9:     T ← StartTemp(E)
10:    n ← 0
11:
12:    while (T_end < T) and (n < n_end) do
13:        while RandomWalkNotDone do
14:            x_2 ← NewConfiguration(x_1)
15:            E_2 ← E(x_2)
16:            if Random(0,1) < exp(−(E_2 − E_1)/T) then
17:                x_1 ← x_2
18:                E_1 ← E_2
19:                if E_1 < E_min then
20:                    x_min ← x_1
21:                    E_min ← E_1
22:                end if
23:            end if
24:        end while
25:        T ← LowerTemperature(T)
26:        n ← n + 1
27:    end while
28:    return x_min
29: end function
```

Figure 5.1: An outline of the simulated annealing algorithm, which takes an objective function E and ending criteria T_{end}, n_{end}. The methods "StartTemp", "RandomWalkNotDone", "NewConfiguration", and "LowerTemperature" are left as general descriptors, to be elaborated on in the coming sections.

5.2 Statistical mechanics

In the simulated annealing algorithm, the "energy" of the system is allowed to vary by a biased random walk, in order to stay within the space of states permitted by T. Or stated in another way, the system is kept in thermal equilibrium with a heat bath of temperature T. In statistical mechanics, such a situation is represented by the canonical ensemble.

In the canonical ensemble, every configuration j in the domain of E represents a microstate, with an assigned probability P by

$$P(j) = \frac{1}{Z} \mathrm{e}^{-E_j/k_b T} \tag{5.2}$$

where E_j is the energy of the state and Z is the partition function of the ensemble. For a discrete configuration space, Z can be written as a sum over all microstates i with energy E_i by

$$Z = \sum_i \mathrm{e}^{-E_i/k_b T}. \tag{5.3}$$

In our case, where all parameters are continuous, this sum would be replaced by an integral, but we will not attempt to compute it.

The important part is that, in the canonical ensemble, two different configurations with energies E_j and E_i will occur with probabilities given by $P(j)$ and $P(i)$, proportional to $\exp(-E_j/k_B T)$ and $\exp(-E_i/k_B T)$ respectively. A system in thermal equilibrium with a heat bath will randomly change its configuration with time, moving from microstate to microstate. For such a process, we may consider the probability that a system in microstate j at one moment switches to microstate i in the next.

Let us denote by $P(i|j)$ the probability of switching to configuration i given that the previous configuration was j. The condition of detailed balance states that it should be as likely to switch to i from a starting point of j, as it would be to switch to j from i. That is,

$$P(i|j)P(j) = P(j|i)P(i). \tag{5.4}$$

which can be rearranged to give

$$\frac{P(i|j)}{P(j|i)} = \frac{P(i)}{P(j)}. \tag{5.5}$$

The transition probability $P(i|j)$ can be factored as a product of two separate probabilities: the probability of proposing i after j, i.e. the proposal probability $g(i|j)$; and the probability of accepting i after j, i.e. the acceptance probability $A(i|j)$,

$$P(i|j) = g(i|j)A(i|j). \tag{5.6}$$

For our algorithm to mimich a system in thermal equilibrium at temperature T, we need a criterion for accepting a suggested next step. That is, it is the acceptance

probability we are interested in finding, and inserting (5.6) into (5.5) we get

$$\frac{P(i)}{P(j)} = \frac{g(i|j)A(i|j)}{g(j|i)A(j|i)} \quad \Leftrightarrow \quad \frac{A(i|j)}{A(j|i)} = \frac{P(i)g(j|i)}{P(j)g(i|j)} \tag{5.7}$$

One might suggest several solutions for $A(i|j)$ to this equation, and in particular it is easy to check that the equation holds when choosing

$$A(i|j) = \min\left(1, \frac{P(i)g(j|i)}{P(j)g(i|j)}\right) \tag{5.8}$$

If we make sure that new configurations are proposed in a manner that is reversible, that is it is as likely to suggest a configuration i from a starting point of j as it is to suggest j from the starting point i, then $g(i|j) = g(j|i)$ and the two cancel out in the expression for $A(i|j)$. Furthermore, in the canonical ensemble the probability of a given configuration is given by its energy and the temperature, satisfying $P(i) \propto \mathrm{e}^{-E_i/k_bT}$, which results in the expression for the acceptance probability that was stated in the previous section,

$$A(i|j) = \min\left(1, \frac{\mathrm{e}^{-E_i/k_bT}}{\mathrm{e}^{-E_j/k_bT}}\right) = \min\left(1, \exp\left(-\frac{E_i - E_j}{k_bT}\right)\right), \tag{5.9}$$

where the partition function Z cancels between the two probabilities.

More generally, the probability of a certain energy E, independent of configuration, is proportional to both e^{-E/k_bT} and the density of states $g(E)$, so that

$$P(E) \propto g(E)\mathrm{e}^{-\frac{E}{k_bT}}. \tag{5.10}$$

By expanding $\ln P(E)$ around $\langle E\rangle$, this can be used to show [27] that the probability distribution E is, to good approximation, a Gaussian with shape

$$P(E) \;\approx\; \mathrm{e}^{-\beta(\langle E\rangle - TS)}\mathrm{e}^{-(E-\langle E\rangle)^2/2k_bT^2C_V} \tag{5.11}$$

where C_V is the heat capacity at constant volume. This fact will be useful to derive a heuristic for the annealing schedule.

It follows that the fluctuation of E is

$$\langle E^2\rangle - \langle E\rangle^2 = k_bT^2C_V, \tag{5.12}$$

which will also be useful to interpret our numerical results. By computing the mean $\overline{E}$ and standard deviation s_E from a random walk, we may estimate the "heat capacity" of our system by

$$C = \frac{s_E^2}{kT^2}. \tag{5.13}$$

The heat capacity will give us much information about requirements on the annealing process, as explained in [26] using the illustration in figure 5.2. For instance, a sudden spike in the heat capacity, as seen in the top of the figure, will require slow annealing to get past that sudden barrier. If, on the other hand, the heat capacity

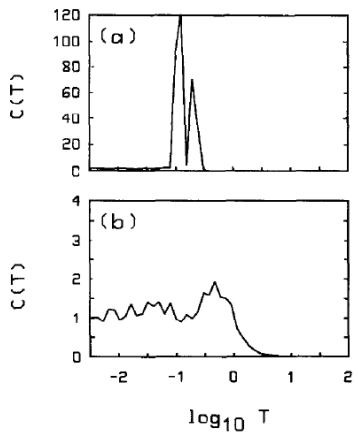

Figure 5.2: Two types of behaviours one might encounter in the heat capacity of a minimised function. Taken from [26, p. 268].

is growing steadily, as seen below in the figure, we do not have to worry as much about controlling the annealing rate.

Our constant k, analogous to the Boltzmann constant k_B, is arbitrary and may be set to 1. In the real world it has the important role of relating energy to temperature, but for our purposes its value will only scale our starting temperature up or down.

5.3 The objective function and its domain

For our purposes, the system configurations are defined by the conductances of our model resistor grid, making E a multivariate function $E(\mathbf{g}) = E(g_1, \ldots, g_M)$ of M variables. The comparison between measurements and model response is done through the measured and modelled transfer matrices A_m and $A(\mathbf{g})$. The objective function may be defined using the norm of their difference,

$$E(\mathbf{g}) \equiv \|A_m - A(\mathbf{g})\|^2 = \sum_{i=1}^{N}\sum_{j=1}^{N} |A_{m,ij} - A(\mathbf{g})_{ij}|^2 . \tag{5.14}$$

In order to keep the problem restricted, all conductances will be assumed to lie in the interval $(1, 10)$, so that $\mathbf{g} \in (1, 10)^M$.

5.4 Generating new steps

The random walk involved in SA requires a generator of new configurations, which are constructed from the current one. If the argument of E is a vector of continuous variables $\mathbf{g}$, as it is in our case this can be phrased as generating steps $\Delta\mathbf{g}$, and

altering the previous state by

$$\mathbf{g}' = \mathbf{g} + \Delta\mathbf{g}. \tag{5.15}$$

The question then becomes how to make optimal choices for $\Delta\mathbf{g}$, a problem that is not to be taken lightly. If the magnitude of the step is too short, the random walk will be very inefficient at exploring the phase space. And at the same time, taking too long steps will make it less likely that a new configuration is accepted.

Then there is also the direction of $\Delta\mathbf{g}$ to consider. In particular, because ERT measurements are more sensitive to surface changes in conductance than changes deep down in the subsurface, we can expect the topmost parameters to be determined before the bottom ones. We therefore would like to see those components of $\Delta\mathbf{g}$ getting smaller in magnitude as T decreases, because otherwise the new configuration is sure to be rejected.

This general problem for minimization by SA of continuous functions is summarized well in Numerical Recipes [25, p. 552]:

> The problem is one of efficiency: A generator of random changes is inefficient if, *when local downhill moves exist*, it nevertheless almost always proposes an uphill move. A good generator, we think, should not become inefficient in narrow valleys, nor should it become more and more inefficient as convergence to a minimum is approached.

The solution proposed by [25] is to use a modified version of the Downhill Simplex Method, in which the rules defining the behaviour of the simplex are rephrased to turn the method into a Metropolis algorithm. This method involves managing $M + 1$ different microstates, rather than just one, all defining a vertex of the simplex. For our purposes, however, this is hugely impractical, as every contraction of the simplex will involve M computations of the transfer matrix. A different scheme is therefore preferred.

A method that seems far more promising is presented by Vanderbilt-Louie in [26], where they describe a self-regulatory mechanism for changing the random step distribution. The method records the K steps of the random walk performed at the previous temperature, and uses its shape to generate steps in the next random walk. The method aims to let the steps conform to the shape of the accessible region of phase space $\Omega(T)$, fuzzily defined as

$$\Omega(T) = \{\mathbf{g} \mid E(\mathbf{g}) - E_{min}(\mathbf{g}) \lesssim T\} \tag{5.16}$$

where $E_{min}(\mathbf{g})$ is the lowest energy in the neighbourhood of $\mathbf{g}$, so that studying the shape of the walk reveals some information about the phase space.

To implement their step generator, the configurations of all accepted positions, $\mathbf{g}^{(k:l)}$ numbered $k = 1, \ldots, K$, are recorded during the random walk at the lth temperature $T^{(l)}$. These are then used to find an the first and second moments of

the random walk, by

$$A_i^{(l)} = \frac{1}{K}\sum_{k=1}^{K} g_i^{(k:l)} \tag{5.17}$$

$$S_{i,j}^{(l)} = \frac{1}{K}\sum_{k=1}^{K}\left(g_i^{(k:l)} - A_i^{(l)}\right)\left(g_j^{(k:l)} - A_j^{(l)}\right). \tag{5.18}$$

The matrix $S^{(l)}$ defined above describes the general shape of the random walk, and therefore also the shape of $\Omega(T^{(l)}$. It can be used to estimate the covariance matrix s^{l+1} at the next temperature, by

$$s^{(l+1)} = \frac{\chi_s}{\beta K} S^{(l)} \tag{5.19}$$

where χ_s is a growth factor typically set equal to 3, and *beta* is given to be 0.11.

Yet another matrix Q is then defined, by

$$s = Q \cdot Q^T, \tag{5.20}$$

which is to say that Q is the Cholesky decomposition of s. Only one more ingredient is then needed; the random vector $\mathbf{u} = (u_1, \ldots, u_M)^T$, whose elements u_i are independent random numbers from a uniform distribution on $(-\sqrt{3}, \sqrt{3})$. The steps $\mathbf{\Delta g}$ generated during the random walk at temperature $T^{(l+1)}$ are then defined by

$$\mathbf{\Delta g} = Q \cdot \mathbf{u}. \tag{5.21}$$

The result will be a new random walk that automatically conforms to the shape of the previous one. For a proper motivation of this rule, see the original paper [26].

The idea is to make the distribution of $\mathbf{\Delta g}$ have the same shape as $\Omega(T)$, which is accomplished provided that the previous random walk has explored the phase space sufficiently well. If two or more variables happen to correlate to a degree, this method will pick up on that tendency, and mimic build this behaviour into the next walk. The suggested steps will then tend to point in the same direction as where there is room to move, even when those directions do not point along any of the many coordinate axes of the system. The goal of the walker should be to get its steps either accepted or rejected about half the time.

The growth factor $\chi_s > 1$ ensures that the walker keeps pushing on the boundary of its current confined region of phase space. This is particularly useful at the start of the annealing, but also in the event of an escape from a local minimum. It can become troublesome however, if $\Omega(T)$ is decreasing in volume too quickly, for instance towards the end of the anneal. Therefore χ_s must not be set too big, and the value $\chi_s = 3$ suggested in [26] would seem to be a good compromise.

As noted in [26], rounding errors may cause problems when small eigenvalues appear in s. Several ways of combating this problem are suggested, but the simplest may be to check the eigenvalues of s before attempting to find Q, and if the the lowest eigenvalue is below a certain threshold, let the random walk go on for another K steps. The value of K must at least be larger than M, so in the numerical experiments, a value $K = 10M$ will be used.

5.5 Annealing schedule

Before the random walk may take place, and before the temperature can be lowered, our method needs a starting temperature. We want, at the start of the method, the temperature to be large enough that virtually any suggested step is accepted, as this is physically equivalent with having a system at an arbitrarily large temperature. That is, we want most energy steps ΔE to be of order T initially.

A good way for finding an appropriate initial temperature, as described in [25], is to take a sufficiently large random sample from the domain of E, and evaluating its sample standard deviation s_E. Because the states were chosen randomly, this can be used to represent a random walk at very high temperature, and s_E for this sample will have the same magnitude as the typical energy step ΔE.

Our method will therefore do exactly this, evaluate s_E for a sample size K of grid vectors $\mathbf{g}$, and let the initial temperature be twice its value.

$$T_{init} = 2s_E \tag{5.22}$$

The initial temperature is not all, however. The annealing schedule itself decides how our method behaves from then on. It consists of two separate but related rules, in that it decides how often and by how much the temperature should be lowered. The first rule boils down to the number of steps required in each random walk, however this has already been addressed in the previous section, where K was set equal to $10M$. The only thing left to decide here is then by how much T should be lowered.

One may encounter many suggested ways of lowering the temperature T between random walks, but not all are very reassuring. Here, a somewhat original but simple scheme will be presented. While it may be possible to find it somewhere in the literature, it has failed to come up in the search related to this work. The scheme to be presented has many appealing qualities, with simple yet convincing motivation.

When the temperature is lowered, so is the mean energy associated with equilibrium state of a system. For a system that was in an equilibrium state at the previous temperature, this can be seen as a perturbation, in a sense proportional to the magnitude of the temperature change. There is no guarantee that the system will be able to regain equilibrium if this perturbation is too severe.

Simulated annealing changes the system in a random walk-like fashion at each new temperature, in an attempt to let the perturbed system regain equilibrium. But if the temperature change is too large or too few successful random steps are made at each temperature, this may fail, causing the system to "freeze" into a local minimum. A safe approach is therefore to change T in small decrements, while taking ample time between each lowering to perform the random walk.

At the same time, a good, quick, and effective simulated annealing algorithm has as its goal to quickly reach the ground state, i.e. the global minimum of f. This necessarily implies lowering T by as much as possible at every step, while also spending a minimal amount time regaining equilibrium before lowering T again. A trade-off is inevitable, and a balance has to be found between the temperature step sizes and the number of successful steps required before continuing.

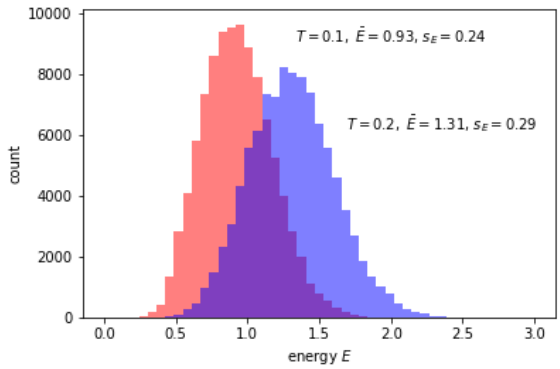

Figure 5.3: Two slightly overlapping histograms of energy, for two separate random walks by the Metropolis algorithm, at two separate temperatures $T = 0.2$ and $T = 0.1$, but using the same energy function. The resulting estimates for the mean energy and variance are labelled.

In figure 5.3 is a histogram of the measured energies of a system performing a random walk at two different temperatures. The distributions are approximately Gaussian, with average energy $\langle E \rangle$ and standard deviation σ, and there is some overlap between them. Ideally, we want the overlap to be as large as possible between one temperature T_1 and the next, T_2, to ensure that a state in equilibrium quickly regains it after being subjected to the change in temperature.

If the temperatures T_1 and T_2 are sufficiently close, the shape and position of their corresponding energy histograms will be similar as well. This notion will give us a reliable way of ensuring a certain overlap in the two histograms. Denote the average energy at temperatures T_1 and T_2 as $\langle E \rangle_1$ and $\langle E \rangle_2$ respectively, and their standard deviations as σ_1 and σ_2.

Assuming for the moment that $\langle E \rangle$ decreases proportionally with T, we have that

$$\frac{T_2}{T_1} = \frac{\langle E \rangle_2}{\langle E \rangle_1} \quad \Leftrightarrow \quad T_2 = T_1 \frac{\langle E \rangle_2}{\langle E \rangle_1} \tag{5.23}$$

which if we want the average energy to decrease by some ϵ, i.e. $\langle E \rangle_2 = \langle E \rangle_1 - \epsilon$, this becomes

$$T_2 = T_1 \frac{\langle E \rangle_1 - \epsilon}{\langle E \rangle_1} = T_1 \left(1 - \frac{\epsilon}{\langle E \rangle_1} \right). \tag{5.24}$$

The size of the overlap between the two distributions can then be set by relating this ϵ to the standard deviations σ_1 and σ_2, for instance by a factor χ_T so that $\epsilon = \chi_T \sigma_1$. This leads to a useful preliminary mechanism for lowering the temperature:

$$T_2 = T_1 \left(1 - \chi_T \frac{\sigma_1}{\langle E \rangle_1} \right). \tag{5.25}$$

Using this expression will require that our method records energies at each temperature T_i, and computes estimates $\overline{E}_i$ and $s_{E,i}$ for $\langle E \rangle$ and σ_E from this

sample at every lowering. This is fortunately not difficult to implement, nor computationally expensive. The actual annealing rate is then decided by

$$T_{i+1} = T_i \left(1 - \chi_T \frac{s_{E,i}}{\overline{E}_i}\right). \tag{5.26}$$

The constant χ_T determines how large the histogram overlap will be, by scaling the temperature step in terms of standard deviations. For instance, if the overlap is to be at 90%, then the value of χ_T can be found from any z-table to be approximately 0.2 [28], a value that has been adopted. If σ does not change too quickly when lowering T by small amounts, this gives us quite precise control over the overlap between the two histograms.

This self regulating annealing rate has as an inbuilt mechanism that it slows down the anneal when it finds that new steps become more difficult to find. If the random walk has wound up in a local minimum, the energy will start to halt, while the variance σ continues to shrink. The anneal then slows down to a crawl, as seen in equation (5.26), where $s_{E,i} \,/\, \overline{E}_i \to 0$ leads to $T_{i+1} = T_i$, giving the method time to find its way out of the local minimum before it is too late.

Chapter 6

Methodology

At this point all the pieces of the puzzle are on the table, and what remains is only to see how well they fit together. However, as was made clear in the previous chapter, simulated annealing is more of a strategy than a fixed and finished algorithm. The list of four elements that one must provide leaves much room for both exploration and potential difficulties, and in what follows there will be plenty of both. A clear methodology is needed in order to proceed.

Several of the parameters involved in the algorithm have until now been kept generally unspecified, such as the grid dimensions N and L, or the precise behaviour of the conductance distribution we want to recover. Their impact on the effectiveness of our algorithm have been explored, and the results are presented in the next chapter.

The resistor grids were displayed as a heatmap of their conductance, in which each node in the grid represented a reqion of the plot. The rectangular shape of the grid was particularly convenient for making such plots.

Every test of the algorithm required a goal for it to aim at. For this purpose, a resistor grid was chosen before each test, to act as a correct answer. The transfer matrix A_m of this "correct grid" was computed from its vector of conductances $\mathbf{g}_m$, by

$$A_m = A(\mathbf{g}_m),$$

and used to define the objective function E from the previous chapter,

$$E(\mathbf{g}) = \|A_m - A(\mathbf{g})\|^2.$$

Knowing the correct answer $\mathbf{g}_m$ allowed for the progress of the algorithm to be recorded using the error

$$e_i = \|\mathbf{g}_m - \mathbf{g}_i\|.$$

An error can also be defined for the grid with lowest energy found so far, by

$$e_{min,i} = \|\mathbf{g}_m - \mathbf{g}_{min,i}\|,$$

where the notation above refers to the lowest energy, not necessarily the lowest *error*.

During the course of the annealing, at each i'th temperature step, several quantities of interest were stored in order to provide more information in the analysis. These quantities included

- the i'th temperature T_i,
- the errors e_i and $e_{min,i}$ mentioned above,
- the average energy $\overline{E}_i$ of the i'th random walk,
- the energy sample standard deviation $s_{E,i}$ of the i'th random walk,
- the heat capacity C_i estimate at the i'th time step, from equation (5.13)
- the cummulative time t_i spent so far,
- the time $\Delta t_i = t_i - t_{i-1}$ spent performing the i'th random walk,
- the cummulative number of attempted and successful steps.

In addition, some snapshots of the grid were stored, for a visual glimpse into the process at different temperatures.

The heat capacity C was explained in the previous chapter to be a useful indicator of difficulty in the annealing. As it increases, it marks an increase in difficulty. Vanderbilt and Louie warned of sudden spikes for some functions [26], which were indicative of temperature regions which would need slow annealing in order to be overcome. The graph of C against T will let us know whether this is the case for our function, and lets us know if any changes should be made to our current annealing schedule. It can be estimated either from our estimates of $\overline{E}_i$ or $s_{E,i}$ along with T_i.

The difficulty of the anneal can also be measured directly from the amount of time Δt_i that is spent performing the i'th random walk. An increase in difficulty implies that the method has a harder time finding accepted steps in the random walk. This in turn leads to more time spent computing transfer matrices that get rejected, which will be evident in a graph of Δt_i.

Graphing the errors e_i and $e_{min,i}$ will let us see at a glance the progress of the algorithm at different temperatures, acting as summaries of the entire annealing. This will give a more objective way of evaluating the algorithm than from looking at plots of the grids for different temperatures.

Another useful quantity is the estimated acceptance probability, which may be found from the recorded number of attempted and successful steps. This will let us know how well the step generator described in the previous chapter actually works. Finally, the annealing rate decided by equation (5.26), i.e. the parenthesis being multiplied by T_i to get T_{i+1}, will be useful in order to judge this particular annealing schedule. As this parenthesis approaches 1, the annealing slows down.

These quantities of interest were all recorded for the different experiments. First, the algorithm was used on simple systems of uniform conductance, to uncover their characteristic behaviour, and how the problem changes with increased grid size. All the data listed above are relevant for this analysis.

As a further test, the algorithm was applied on a grid with non-uniform conductance of appropriate size, to investigate the level of detail that might be recovered. This also served to investigate whether a phenomenon seen in the grids with uniform conductance was specific to those grids, or a problem related to the discretization itself.

Chapter 7

Results

In this chapter, the results of the numerical experiments will be presented. First, the results from grids with uniform conductance, for different grid sizes. The behaviour of the smallest grid will also be explored in more detail, before moving on to the larger ones.

Finally, a grid with more complicated conductance distribution is explored, to see how this affects the performance of the algorithm.

7.1 Uniform conductance

An experiment was run to invert the measurements of a 10-by-3 grid of uniform nodal conductance of value $g_n = 5.5$. Using the SA algorithm, an initial temperature was found and then gradually lowered by a factor 10^{-12}. The resulting change in the grid during this experiment is presented in figure 7.1.

Note that a checkerboard-pattern starts to form in the grid, interchanging between values slightly higher and slightly lower than the goal. However, the checkerboard is not entirely consistent in the first few pictures, and a kind of geometric frustration appears to take place, with interfaces between the two different patterns. There seem to be separate contending choices for which nodes should be higher and which should be lower, but in the end one of them wins before slowly fading out.

This pattern may be an artefact of the chosen discretization. This sort of variation is a consequence of distributing the conductance values at each node rather than each resistor. Two neighbouring nodes are able to cancel eachothers error in their shared resistor by compensating in opposite directions from the correct value. This is approximately true, but as the temperature is lowered further, even this error is smothened out. It will be interesting to see if this problem persists in the larger grids, and more interesting still in the case of non-uniform conductance. It may be that this behaviour is not only a consequence of the choice in discretization, but also the high degree of symmetry in the conductance of the grid.

This precise behaviour may in part be due to the chosen new-step generator. As

was explained in chapter 5, steps are generated based on the previous behaviour, attempting to mimic the phase of the phase space. As the temperature is lowered very far, this method seems here to sniff out the one degree of freedom still available to it once the rest are gone, being this checkerboard patterned variation.

The total error of the grid is shown in figure 7.2, both the instantaneous and the error of the grid with least energy yet encountered. An overall downward trend can be seen, although with many bumps and stagnant intervals. The bumps may be due to the geometric frustration mentioned above. These interfaces must disappear before the grid can progress down to a lower energy level, in much the same way as real physical systems that experience frustration have to do as well. The different contending regions are gradually defeated by the final pattern, and each defeat results in a lower energy being made available, as well as a lower error in the grid.

In figure 7.3 can be seen the heat capacity of the system being annealed. While the behaviour is erratic, even that of the smoothed moving average, it appears to be growing steadily up to a plateau. This is comforting, with respect to the characterisations discussed in chapter 5, as it implies a lack of any sudden barriers in the problem that have to be looked out for. We instead face multiple smaller barriers, in the form of the frustration described above, which may explain the many peaks of the smoothed heat capacity.

The difficulty does increase, however, as the heat capacity rises. This is seen in the time plots of figure 7.4, where an extrapolated trend for further annealing appears to be exponential. We also see clearly in the graph of Δt_i at what moment the eigenvalues of s become too small. The method then require an additional K random steps to be recorded, resulting in a jump. This is what drives the time of the method up, and only this, as seen in the estimated acceptance probability to the right in the figure. From that point on, the probability evens out around $p \approx 0.5$.

The average energy and sample standard deviation are plotted to the left in figure 7.5. We observe a steadily decreasing s_E, and a comparable but slightly more bumpy $\overline{E}$ just above it. The annealing rate is plotted to the right in the same figure, and demonstrates the advantage of using the annealing schedule derived in chapter 5. As the annealing difficulty increases, the temperature steps become smaller. Note that the bumps that can be seen in the annealing rate coincide with those in the average energy, where the method seems to start to get stuck. This is the desired behaviour, as by letting the rate grow closer to 1 in these regions, the next temperature step will be small, giving the method a chance to find a way out of the trap in which it seems to have been caught.

Two more experiments were performed for uniform conductance, on grid sizes 15-by-5 and 20-by-7. In both cases, the temperature was lowered by a factor 10^{-8} before completion. The end result of the inversion is shown in figures 7.6, along with plots of the expended time t_i and estimated acceptance probability. The algorithm took 463.5 seconds to produce the 15-by-5 grid, i.e. 7 minutes and 43.5 seconds, and 40072.1 seconds on the 20-by-7 grid, i.e. 11 hours, 7 minutes, and 52.1 seconds. These numbers are much larger than for the smaller case, despite the fact that the end temperatures here are proportionally higher by a factor of 10^4.

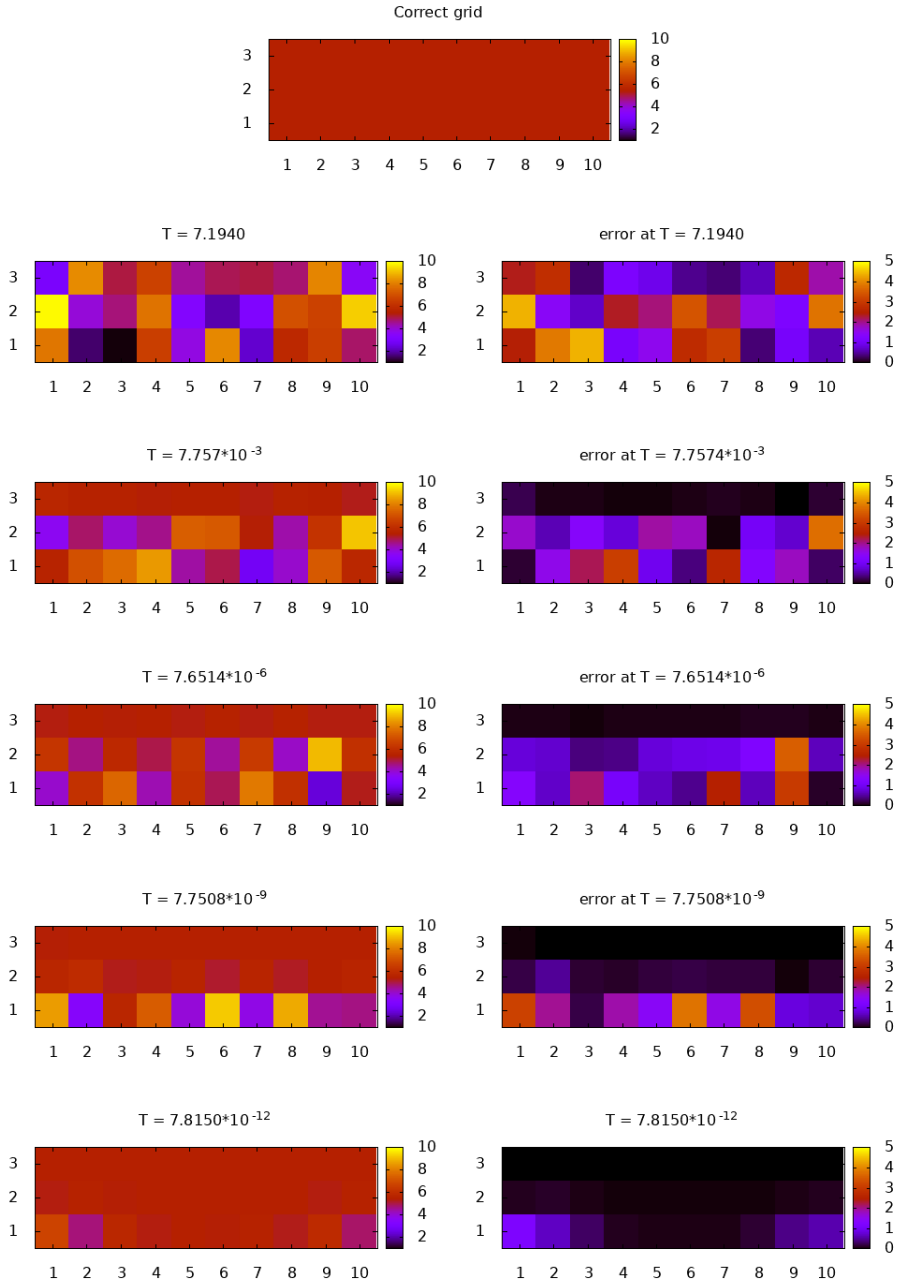

Figure 7.1: Snapshots of the grid conductance at different stages of the annealing, starting at $T = 7.677$, and ending at $T = 5.182 \cdot 10^{-7}$. The correct grid is at the top, the estimate at decreasing T is in the left column, and the error is plotted to the right.

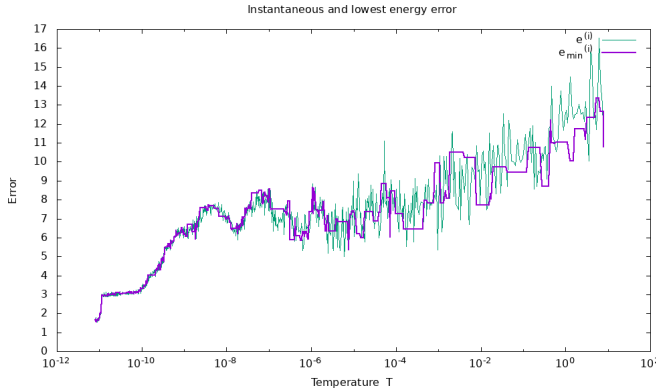

Figure 7.2: The error during the annealing process. The error of the instantaneous state of the grid is shown in light blue, while the error of the grid with the lowest energy yet encountered is shown in purple.

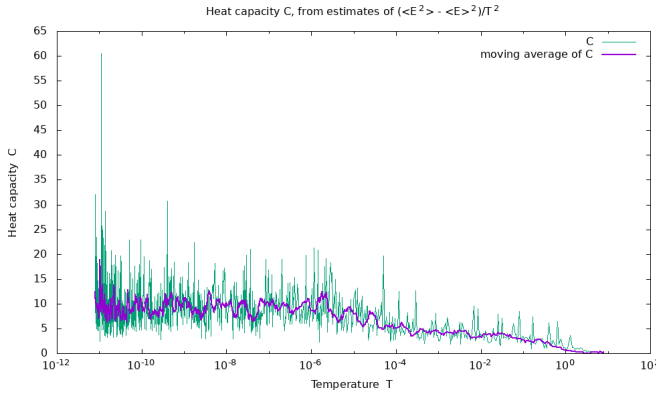

Figure 7.3: The heat capacity of the system as the temperature is lowered. Both the instantaneous estimate of C and its moving average are shown, to somewhat reduce the erratic behaviour that follows from the use of rough estimates. The increase in difficulty appears steady with decreasing temperature.

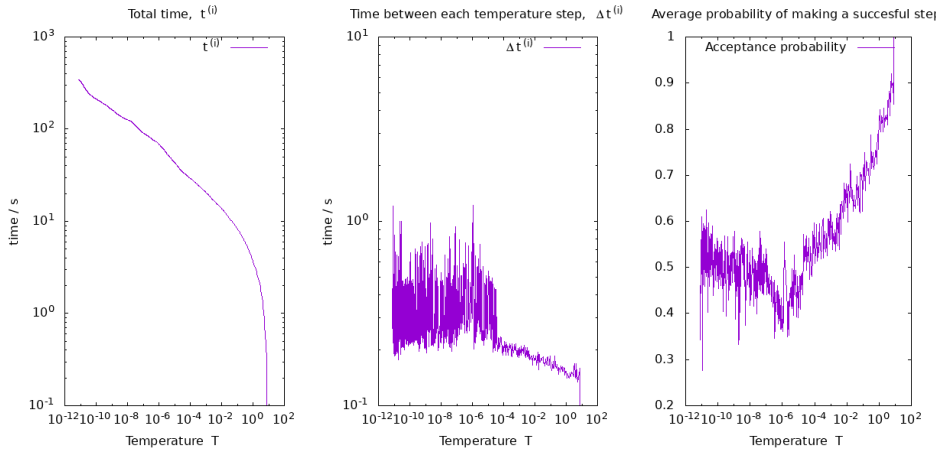

Figure 7.4: Graphs of the time usage in the first inversion. To the left is the cumulative time spent by the algorithm, which indicates an exponential trend for further annealing. In the middle is the time spent in each random walk. To the right is the estimated acceptance probability.

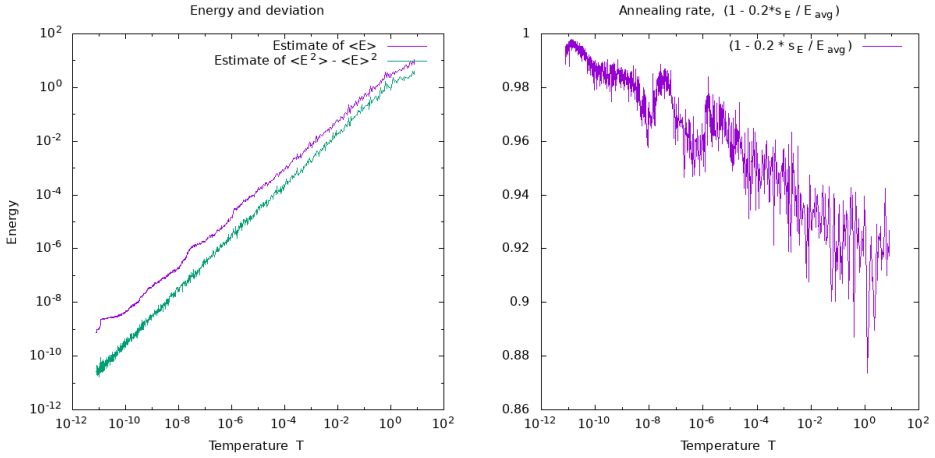

Figure 7.5: To the left, graph of the average $\overline{E}_i$ and sample standard deviation $s_{E,i}$, used to estimate $\langle E \rangle$ and σ_E. These also decide the annealing rate, which is plotted to the right.

Our algorithm seems to have a harder time with these larger grids than it did with the smaller one. Note again the appearance of a checker board pattern in the conductance of both these grids, but more clearly than in the previous experiment. While these final grids may appear more chaotic than the final grid before, their errors are relatively low throughout the grid. This lends credence to the interpretation that the checker board pattern arises because of neighbouring nodes having smaller and larger conductances than the correct value end up cancelling each other out.

In the error plots for each grid, spread in around the purple nodes, there are also spots and blemishes of higher error. These are reminiscent of the imperfections seen in metals and crystals, where the desired lattice structure exhibits a glitch in the typical pattern. This similarity is very potent, and may in fact tell us that the implemented method has progressed too quickly down to lower temperatures, resulting in these very same glitches in our resistor grid "crystal".

7.2 Grid with non-uniform conductance

A fourth experiment was performed on a grid of size 12-by-4, but with a non-uniform conductance. This size was chosen due to the long times that were needed for the two larger grids, and because of the exceptionally good performance of the smallest. The shape of the goal conductance was chosen to mimic a layered subsurface with also some horizontal variation. The result of this experiment is shown in figure 7.7 along with a graph of the annealing time, which ends at 438.9 seconds, i.e. 7 minutes and 18.9 seconds.

The error plots in the same figure show that, not only does the final picture look similar, but there also seems to be no sign of the checker board pattern that so plagued the uniform conductances. The problem does therefore seem to have been in the high level of symmetry in the conductance distribution, as well as the chosen discretization.

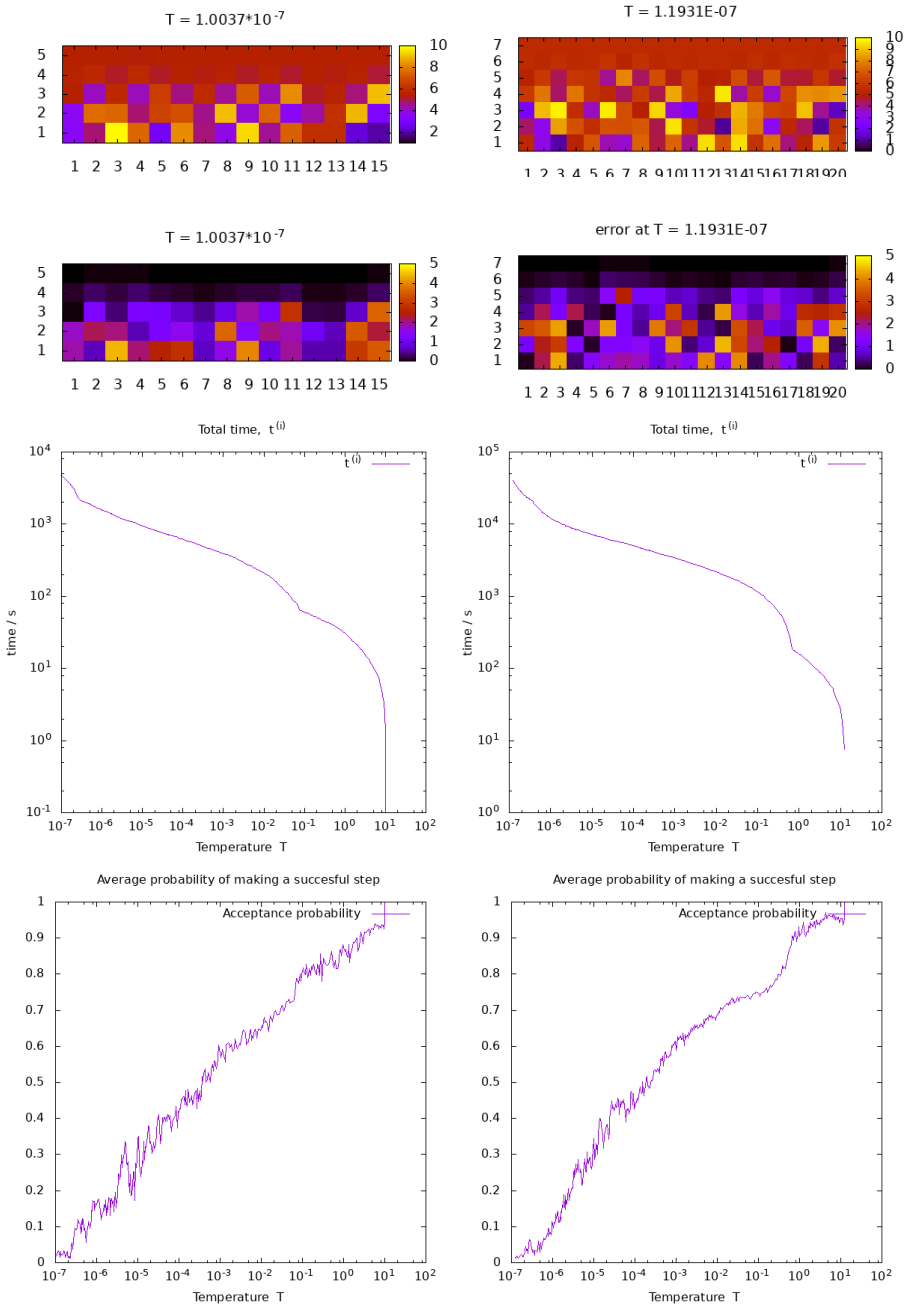

Figure 7.6: The result of the 15-by-5 (left) and 20-by-7 (right) uniform conductance trials, both final grids and their error, along with plots of the time t_i and acceptance probabilities at different temperatures T_i. In both cases, the time cost of the algorithm starts to reach extreme proportions towards the end, but now due to a vanishing acceptance probability.

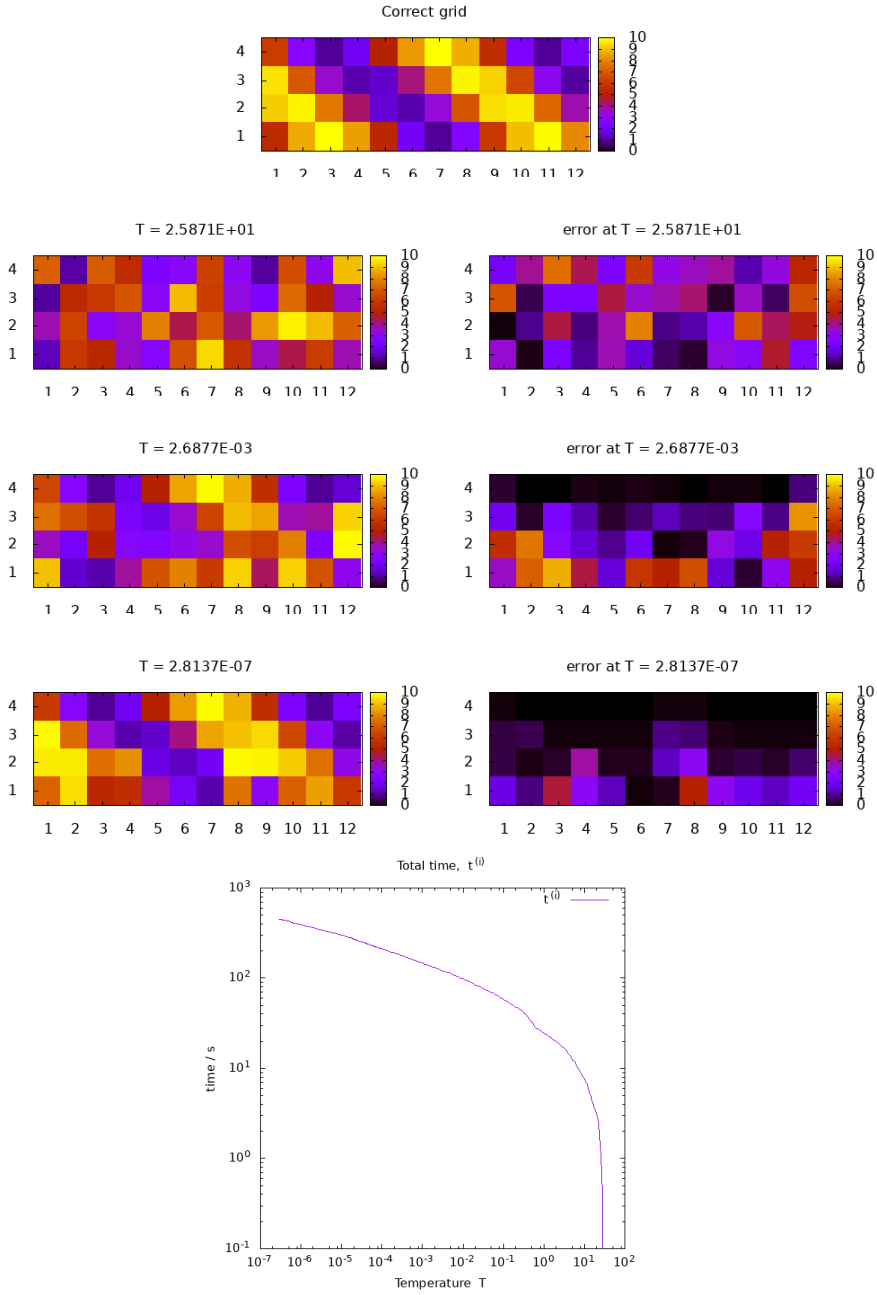

Figure 7.7: The result of the final trial, with non-uniform conductance on a grid with dimensions 12-by-4. The final result looks strikingly similar to the goal, but the error shows us that there is still some way to go.

Chapter 8

Discussion and Conclusion

The simulated annealing method definitely shows promise. In all four of the grids that were studied, the method was able to find grids that were in some sense close to the correct answer.

The problems that were encountered were all associated with our specific implementation of SA, rather than the concepts underpinning it as a minimisation algorithm. It therefore still warrants further research, to investigate whether the shortcomings of this work can be overcome by making different choices in discretization, step generator, as well as the objective function and conductance distribution.

We observed a checker board like pattern emerging in the grids with uniform conductance. This pattern appeared to be an artefact of the way the subsurface was discretized in chapter 3, combined with the self regulating step generator that was chosen in chapter 5, merging in a sort of perfect storm when applied to the uniform conductance grids. It is possible that changing either one of these three componenets might solve the problem. The effect was observed to go away once the conductance distribution was swapped with one of lower symmetry.

In future work on this problem, a wise place to start would be to find a different way of discretizing the subsurface. Either still using resistor grids, but then choosing a critical and convenient graph other than the one used in this work, or by applying SA to the block-model used by the RES2DINV program.

Another area of improvement is the step generator. While it did behave as intended, the previous chapter clearly demonstrates that conforming with the shape of the previous random walk may lead to undesirable feedback loops. More work is therefore needed to determine if this method can be augmented to account for such cases as the ones seen here, though they may be somewhat pathological.

It was however pleasing to see the success of the annealing schedule, derived in chapter 5. While problems did appear in many parts of the implementation, the annealing schedule behaved as expected and without issue. The annealing rate was observed to slow down with increasing difficulties, and accelerate again when able, but overall slowing down gradually. This let our method spend less time in the higher temperatures, where only low level details manifest, and spend more time at lower temperatures, where the precise picture is painted.

Apart from these questions of implementation, the choice of objective function may also be questioned. It is not at all certain that the norm of the matrix difference in (5.14) is the optimal way of using the information contained in the transfer matrix A. While the simulated annealing method may perform well against difficult problems, there is no reason to make it more difficult than necessary.

For instance, the function may be replaced by the sum of square difference between measured and simulated apparent resistivities. These may be computed from A, as shown in chapter 3. This would bring us closer to the true 3D ERT problem, if accompanied by a model that also describes 3D measurements.

Our results say nothing, however, about how SA will perform for more wide ranging conductance values. Because the conductance may vary with several orders of magnitude, our experiments are limited also by the fact that they restrict all conductances to the interval $(1, 10)$. It is not certain how the SA method will perform against more general conductance ranges, so more research is certainly needed in this respect as well.

8.1 Conclusion

In conclusion, after several chapters of theory and buildup, the numerical experiments have taught us a great deal. Specifically, simulated annealing does appear to have great potential in this problem as a minimisation technique, but is here impeded by problems in its specific implementation.

However, there are still questions that remain unanswered, several arising from the results that were obtained in this work. For instance, more research is needed to find a well suited step generator. In addition, and perhaps even more importantly, a better way is needed of discretizing the subsurface, which does not carry with it any pitfalls like the geometric frustration that we observed.

In short, this thesis does not produce any clear answer to its very actual question. In order to say confidently to what extent exactly SA performs better or worse than the inversion techniques currently in use, we may only conclude that further research is needed.

Bibliography

[1] M. H. Loke. *Tutorial : 2-D and 3-D electrical imaging surveys*. Geotomo Software. Mar. 2015.

[2] Alberto P. Calderón. "On an inverse boundary value problem". In: *Seminar on Numerical Analysis and its Applications to Continuum Physics* (1980), pp. 65–73.

[3] Gunther Uhlmann. "30 Years of Calderón's Problem". In: *Séminaire Laurent Schwartz — EDP et applications* 2012-2013 (2012), pp. 1–25.

[4] Fernando Guevara Vasquez Liliana Borcea Vladimir Druskin and Alexander V. Mamonov. "Resistor network approaches to electrical impedance tomography". In: *Inside Out II* 60 (2012), pp. 55–118.

[5] Olavo H. Menin and Chris T. Bauch. "Solving the patient zero inverse problem by using generalized simulated annealing". In: *Physica A: Statistical Mechanics and its Applications* 490 (2018), pp. 1513–1521. ISSN: 0378-4371. DOI: https://doi.org/10.1016/j.physa.2017.08.077. URL: http://www.sciencedirect.com/science/article/pii/S0378437117308014.

[6] Ranjan Das. "Application of Simulated Annealing for Inverse Analysis of a Single-Glazed Solar Collector". In: *Advances in Intelligent Informatics*. Ed. by El-Sayed M. El-Alfy et al. Cham: Springer International Publishing, 2015, pp. 267–275. ISBN: 978-3-319-11218-3.

[7] Alexandre Timonov and Michael V. Klibanov. "An Efficient Algorithm for Solving the Inverse Problem of Locating the Interfaces Using the Frequency Sounding Data". In: *Journal of Computational Physics* 183.2 (2002), pp. 422–437. ISSN: 0021-9991. DOI: https://doi.org/10.1006/jcph.2002.7200. URL: http://www.sciencedirect.com/science/article/pii/S0021999102972001.

[8] Douglas John Moseley. "Computational Solution Of Inverse Problems With Simulated Annealing". In: *Digitized Theses* 2567 (1995). URL: https://ir.lib.uwo.ca/digitizedtheses/2567.

[9] Ruden AS. *Ruden AS Geo solutions*. 1999. URL: http://www.rudenas.com/ (visited on 04/27/2018).

[10] H. F. Morrison A. Dey. *Resistivity modelling for arbitrarily shaped two-dimensional structures*. Vol. 27. 1. European Association of Exploration Geophysicists, 1979, pp. 106–136.

[11] John Sylvester and Gunther Uhlmann. "A Global Uniqueness Theorem for an Inverse Boundary Value Problem". In: *Annals of Mathematics* 125.1 (1987), pp. 153–169. ISSN: 0003486X.

[12] Kari Astala and Lassi Päivärinta. "Calderón's inverse conductivity problem in the plane". In: *Annals of Mathematics* 163 (2006), pp. 265–299.

[13] Giovanni Alessandrini. "Determining Conductivity by Boundary Measurements, the Stability Issue". In: *Applied and Industrial Mathematics - Mathematics and its Applications* (1988), pp. 317–324.

[14] Giovanni Alessandrini and Sergio Vessella. "Lipschitz stability for the inverse conductivity problem". In: *Advances in Applied Mathematics* 35 (2005), pp. 207–241.

[15] Luca Rondi. "A remark on a paper by Alessandrini and Vessella". In: *Advances in Applied Mathematics* 36.1 (2006), pp. 67–69. ISSN: 0196-8858. DOI: https://doi.org/10.1016/j.aam.2004.12.003. URL: http://www.sciencedirect.com/science/article/pii/S019688580500093X.

[16] Gunther Uhlmann Oleg Yu. Imanuvilov and Masahiro Yamamoto. "The Calderón problem with partial data". In: *J. Amer. Math. Soc.* 23 (2010), pp. 655–691. DOI: https://doi.org/10.1090/S0894-0347-10-00656-9.

[17] Johannes Sjöstrand Carlos E. Kenig and Gunther Uhlmann. "The Calderón problem with partial data". In: *Annals of Mathematics* 165 (2007), pp. 567–591.

[18] J. Vannimenus B. Derrida J. G. Zabolitzky and D. Stauffer. "A Transfer Matrix Program to Calculate the Conductivity of Random Resistor Network". In: *Journal of Statistical Physics* 36 (1984), pp. 31–42.

[19] Liliana Borcea, Vladimir Druskin, and Fernando Guevara Vasquez. "Electrical impedance tomography with resistor networks". In: *Inverse Problems* 24.3 (2008), p. 035013. URL: http://stacks.iop.org/0266-5611/24/i=3/a=035013.

[20] Edward B. Curtis and James A. Morrow. *Inverse Problems for Electrical Networks*. URL: https://sites.math.washington.edu/~curtis/book.pdf (visited on 05/25/2018).

[21] Murthy N. Guddati Sergey Asvadurov Vladimir Druskin and Leonid Knizhnerman. *On optimal finite-difference approximation of PML*. Vol. 41. 1. Society for Industrial and Applied Mathematics, 2003, pp. 287–305.

[22] J. A. Morrow E. B. Curtis D. Ingerman. *Circular planar graphs and resistor networks*. Vol. 283. 1998, pp. 115–150.

[23] B. Derrida and J. Vannimenus. "A transfer-matrix approach to random resistor networks". In: *Journal of Physics A: Mathematical and General* (1982), pp. 557–564.

[24] S.I. Kabanikhin. *Inverse and Ill-posed Problems: Theory and Applications*. Inverse and Ill-Posed Problems Series. De Gruyter, 2011. ISBN: 9783110224016. URL: https://books.google.no/books?id=W7jPfhwAlcEC.

[25] William H. Press et al. *Numerical Recipes 3rd Edition: The Art of Scientific Computing*. 3rd ed. New York, NY, USA: Cambridge University Press, 2007.

[26] D. Vanderbilt and S. G. Louie. "A Monte Carlo Simulated Annealing Approach to Optimization over Continuous Variables". In: *Journal of Computational Physics* 56 (Nov. 1984), pp. 259–271. DOI: 10.1016/0021-9991(84)90095-0.

[27] Jens O. Andersen. *Introduction to Statistical Mechanics*. 1st ed. Trondheim, Norway: Akademika forlag, 2012. ISBN: 978-82-321-0105-4.

[28] Jan Terje Kvaløy and Håkon Tjelmeland. *Tabeller of formler i statistikk*. Vigmostad og Bjørke AS, 2000. ISBN: 8251915953.

[29] Rhett Herman. "An introduction to electrical resistivity in geophysics". In: *American Journal of Physics* 69.9 (2001), pp. 943–952. DOI: 10.1119/1.1378013.

Appendices

Appendix A

The geometric constant k

A four-point measurement of ρ_a involves passing a current I in and out of two of the points on $\partial\Omega$, and measuring the resulting potential difference V between the other two points. (FIGUR) If ρ were uniform in Ω, it would be possible to calculate it from I and V, provided the shape of Ω and the relative position of the points were known as well. Fortunately, because geophysics typically involves the flat ground with negligible curvature, a decent approximation is to let the surface be the xy-plane, and the subsurface be the entire region with negative z.

The advantage of this approximation is that, for a homogeneous medium of equivalent shape, we do know how to compute ρ. First, for a single point-like source of current I at location $\mathbf{x}'$, the current vector $\mathbf{J}$ satisfies

$$\nabla \cdot \mathbf{J}(\mathbf{x}) = 2I\delta(\mathbf{x} - \mathbf{x}'), \tag{A.1}$$

where a multiplication by 2 has taken place due to all the current flowing into only one half of the conducting region. Expressing $\mathbf{J}$ in terms of u and σ, we get for homogeneous media

$$\nabla \cdot (-\sigma \nabla u)(\mathbf{x}) = 2I\ \delta(\mathbf{x} - \mathbf{x}') \tag{A.2}$$

$$\nabla^2 u(\mathbf{x}) = -2I\rho\ \delta(\mathbf{x} - \mathbf{x}') \tag{A.3}$$

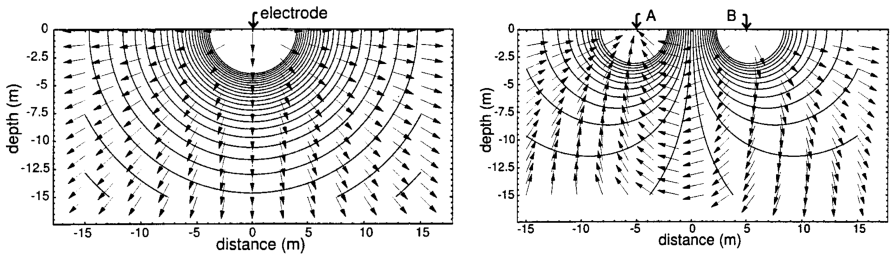

(a) One current electrode **(b)** Two electrodes, opposite currents

Figure A.1: The potentials and current fields for one and two electrodes.[29]

which has solution

$$u(\mathbf{x}) = \frac{I\rho}{2\pi}\frac{1}{|\mathbf{x}-\mathbf{x}'|}, \tag{A.4}$$

as illustrated in figure A.1a.

If we now instead consider two point-like sources of current, of strength I and $-I$ at locations $\mathbf{x}_{C1}$ and $\mathbf{x}_{C2}$, the total potential becomes the sum of their individual potentials as given above,

$$u(\mathbf{x}) = \frac{I\rho}{2\pi}\left(\frac{1}{|\mathbf{x}-\mathbf{x}_{C1}|} - \frac{1}{|\mathbf{x}-\mathbf{x}_{C2}|}\right), \tag{A.5}$$

as illustrated in figure A.1b.

From this we can easily find an expression for the potential drop V between two points $\mathbf{x}_{P1}$ and $\mathbf{x}_{P2}$. Renaming the distances $|\mathbf{x}_A - \mathbf{x}_B|$ as r_{AB}, we get

$$\begin{aligned} V &= u(\mathbf{x}_{P1}) - u(\mathbf{x}_{P2}) \\ &= \frac{I\rho}{2\pi}\left(\frac{1}{r_{C1P1}} - \frac{1}{r_{C2P1}} - \frac{1}{r_{C1P2}} + \frac{1}{r_{C2P2}}\right), \end{aligned}$$

which can be rearranged to give us, as was stated in the opening chapter,

$$\rho = k\frac{V}{I}. \tag{A.6}$$

The value of the geometric factor k is then evidently

$$k = 2\pi\left(\frac{1}{r_{C1P1}} - \frac{1}{r_{C2P1}} - \frac{1}{r_{C1P2}} + \frac{1}{r_{C2P2}}\right)^{-1}, \tag{A.7}$$

and depends only on the relative distance between measurement points. This is what is meant by the apparent resistivity ρ_a, when measured by a quadripole array.

Appendix B

Transfer matrix, one resistor at a time

Instead of calculating the transfer matrix A entire layers at a time, it is possible to derive a procedure from the two equations (4.8a) and (4.8b), by which we can compute the change in A as a single resistor is added.

First, adding to a square grid one single vertical resistor with conductance g at position α is equivalent to adding a whole vertical layer, where all resistors besides α have infinite conductance.

These infinite conductances cadically simplify the expression for adding a layer of vertical resistors, $A' = A(I + V^{-1}A)^{-1}$. Notice that the diagonal matrix V^{-1} with n'th main diagonal element is $1/v_n$ now contains mostly zeros, except element (α, α) which is equal to $1/g$.

$$V = \begin{pmatrix} & & \\ & 1/g & \\ & & \end{pmatrix} \tag{B.1}$$

The product $V^{-1}A$ is therefore mostly zeros, except row number α, which will have in column n elements given by $\frac{a_{\alpha,n}}{g}$. Adding this to I is therefore

$$I + V^{-1}A = \begin{pmatrix} 1 & & & & & \\ & \ddots & & & & \\ \frac{a_{\alpha,1}}{g} & \cdots & 1 + \frac{a_{\alpha,\alpha}}{g} & \cdots & \frac{a_{\alpha,N}}{g} \\ & & & \ddots & \\ & & & & 1 \end{pmatrix} \tag{B.2}$$

Finding the inverse $(I + V^{-1}A)^{-1}$ of this matrix can be done by hand. Each row operation in the Gauss-Jordan elimination will involve subtracting $\frac{a_{\alpha,m}}{g}$ times row m from row α, before finally dividing row α by $1 + \frac{a_{\alpha,\alpha}}{g}$. Note only that we may

write

$$\left(1+\frac{a_{\alpha,\alpha}}{g}\right)^{-1} \;=\; \frac{g}{g+a_{\alpha,\alpha}} \;=\; 1-\frac{a_{\alpha,\alpha}}{g+a_{\alpha,\alpha}}, \tag{B.3}$$

resulting in

$$\left(I+V^{-1}A\right)^{-1} \;=\; \begin{pmatrix} 1 & & & & \\ & \ddots & & & \\ \frac{-a_{\alpha,1}}{g+a_{\alpha,\alpha}} & \cdots & 1-\frac{a_{\alpha,\alpha}}{g+a_{\alpha,\alpha}} & \cdots & \frac{-a_{\alpha,N}}{g+a_{\alpha,\alpha}} \\ & & & \ddots & \\ & & & & 1 \end{pmatrix} \tag{B.4}$$

As we see, this inverse can be written in component form as

$$\left[\left(I+V^{-1}A\right)^{-1}\right]_{i,j} = \delta_{i,j} - \delta_{i,\alpha}\frac{a_{\alpha j}}{g+a_{\alpha\alpha}} \tag{B.5}$$

Multiplying this in with A will then finally yield

$$[A']_{i,j} = \left[A\left(I+V^{-1}A\right)^{-1}\right]_{i,j} \tag{B.6}$$

$$a'_{i,j} = \sum_k a_{i,k}\left(\delta_{k,j} - \delta_{k,\alpha}\frac{a_{\alpha j}}{g+a_{\alpha\alpha}}\right) \tag{B.7}$$

$$= \sum_k \left(a_{i,k}\delta_{k,j} - a_{i,k}\delta_{k,\alpha}\frac{a_{\alpha j}}{g+a_{\alpha\alpha}}\right) \tag{B.8}$$

$$= a_{i,j} - \frac{a_{i,\alpha}a_{\alpha j}}{g+a_{\alpha\alpha}} \tag{B.9}$$

The formula for adding a single horizontal resistor from node β to node γ is trivial to derive from the formula for adding a layer of horizontal resistors in equation (4.8a). We can easily set all except one horizontal resistors to zero conductance in the matrix H, leading to a matrix with terms in only the four positions (β,β), (β,γ), (γ,β), (γ,γ). The resulting change in A will be given by

$$a'_{i,j} = a_{i,j} + \begin{cases} g & \text{if } i=j=\alpha \qquad\qquad \text{or } i=j=\alpha+1 \\ -g & \text{if } i=\alpha,\ j=\alpha+1 \quad \text{or } i=\alpha+1,\ j=\alpha \end{cases} \tag{B.10}$$

or written in another way,

$$a'_{i,j} \;=\; a_{i,j} + g(\delta_{i,\alpha}-\delta_{i,\alpha+1})(\delta_{j,\alpha}-\delta_{j,\alpha+1}) \tag{B.11}$$

Of these two expressions I prefer the first one when it comes to understanding how it can most easily be implemented, but the second is admittedly tidier.

If we take a step back to look at this final result, it makes a lot of sense in light of the "equivalent web-like grid" interpretation from chapter 3. If the elements of A can be considered the conductance values of such an equivalent grid, then

adding another sideways resistor is nothing more than creating a parallel coupling between the two nodes. Since we are talking about conductances, the total new value will just be their sum, and none of the other resistors are affected. In A, this is to subtract the conductance g at the positions (β, γ),(γ, β), and adding it to the diagonal entries of the corresponding rows so that the row-sum is still 0.